UC Davis
UC Davis Electronic Theses and Dissertations

Title

Numerical Simulation of Multiphase Electrohydrodynamic Flow Under Uniform Electric Fields

Permalink

https://escholarship.org/uc/item/43z116wd

Author

Karam Padilla, Jorge

Publication Date

2023

Peer reviewed|Thesis/dissertation

Numerical Simulation of Multiphase Electrohydrodynamic Flow Under Uniform Electric Fields

By

JORGE ABRAHAM KARAM PADILLA

THESIS

Submitted in partial satisfaction of the requirements for the degree of

MASTER OF SCIENCE

in

Mechanical and Aerospace Engineering

in the

OFFICE OF GRADUATE STUDIES

of the

UNIVERSITY OF CALIFORNIA

DAVIS

Approved:

_____

Jean-Pierre Delplanque, Chair

_____

Stephen K. Robinson

_____

Mohamed M. Hafez

Committee in Charge

2024

Table of Contents

Table of Figures

Abstract

In recent years, electrohydrodynamic flow applications have gained popularity due to their ability to control flow characteristics by subjecting them to an electric field. A prime example of this is electrospray thruster for electric propulsion applications. The useful ability to carefully control the operating regimes of an electrospray device with properties such as flow rate and voltage has proved beneficial for the small satellite industry.

With the use of the open-source software OpenFOAM, a numerical solver capable of successfully capturing multiphase electrohydrodynamic phenomena has been implemented. The solver takes advantage of the existing OpenFOAM infrastructure to couple the dynamic interplay between electric fields and fluid dynamic. The numerical simulations employ sophisticated algorithms to elucidate the intricate behavior of charged droplets, shedding light on key parameters such as cone-jet length, jet diameter, and droplet diameter. Additionally, a selection of validation test cases is showcased to assess the solver's accuracy and validity. In this work, electrospray simulations with varying liquid flow rate and applied voltages are presented. With heptane as the working fluid, results show that the solver produces comparable results to those simulated by competing numerical approaches. Moreover, the results from these simulations demonstrate satisfactory agreement with both experimental data and analytical solutions. Qualitatively, the simulations performed in this study accurately show the cone-jet formation and breakup of droplets normally seen in experimental works. By competently simulating electrospray phenomena in the steady cone-jet regime, this research contributes valuable insights that can inform the design and optimization of electrospray systems in various applications, spanning from drug delivery to electric propulsion.

Acknowledgments

Sometimes I sit around and think where I would be if it was not for the people that have been part of this journey. To my parents, I am forever indebted for your constant loving and support. Without your sacrifices, none of this would be possible. Because of you, I am who I am today. Now I look back and realize that every single sacrifice we have made as a family has been a blessing in disguise. To my siblings, Gaby, Sebastian, and Santiago. Your love, resiliency, and constant fight in what you all do have fueled me to continue chasing my dreams. I am truly blessed to be able to share a life and a family with you. Gracias por ser mi motor. Los amo con todo mi corazón.

I would like to thank Prof. Delplanque for his invaluable advice, mentorship, and constant patience. I am beyond grateful for everything he has done to support my success: from welcoming me into UC Davis with open arms to nurturing my curiosity day in and day out. I do not have enough words to express my gratitude. Additionally, I would like to thank Prof. Robinson and Prof. Hafez for their valuable role in my thesis completion. Your counsel and wisdom have fostered my growth as a researcher. Both are true role models in the aerospace and mechanical field.

To the Delplanque Research group, I truly admire your hard work and capacity to overcome the obstacles that come with being a student in graduate school. The academic conversations we shared provided insightful ideas that allowed me to further my learning experience. To Dr. Carlos Ruvalcaba, I could have not asked for a better mentor. I am forever thankful for the countless times you took time out of your day to help me. Your friendship and advice are things that I will cherish for the rest of my life. To Tim Linke, your positivity and intelligence have always inspired me. When things got difficult, you always taught me to look at the bright side.

To the UC LEADS community: Mariela Menendez, Lynne Arcangel, and Manuel Paul. Thank you for your constant guidance and for sincerely believing in my abilities. You have made my graduate journey

a genuine one. Joining UC LEADS has been one of the best decisions of my entire academic career. Without this community, it would be difficult to picture myself at this instance of my life.

To the friends I have made during my time in Davis: Niko, Varun, Meridian, Alejandro, Randi, Tim, David, and Nayarit. Thank you for being the great friends you are. You are my family far from home. You have made my time in Davis an unforgettable one.

Without a doubt, I have been privileged to further my education at the University of California, Davis. Being a student at this institution has allowed me to grow as an aerospace engineer, and most importantly, as a person. It is difficult to put into words what the last couple of years have meant to my development.

I. Introduction

Electrospray phenomena are deeply rooted in the physical principles of electrohydrodynamics (EHD), a field that combines the dynamics of fluids with the discipline of electrostatics. By its strict definition, electrospray phenomena refer to the emission of fine droplets from a liquid surface under the effects caused by an electric field. This phenomenon has found applications in several fields such as materials science, medicine, mass spectroscopy, and most prominently, electric propulsion for space applications [1–3]. The need for alternative propulsion systems has sparked new interest in the study of electrospray phenomena.

A fundamental aspect of the electrospray process is the formation of what is known as the Taylor Cone. As a liquid is subjected to an electric field, the balance between electric and surface tension forces at the liquid's surface results in the formation of a cone, first described by Sir Geoffrey Taylor in 1964 [4]. As the cone elongates, a fine liquid jet is emitted from its apex. The jet experiences a sequence of instabilities, leading to the formation of smaller droplets through a process known as the Rayleigh instability [5]. The final outcome is a multitude of highly charged, monodisperse droplets.
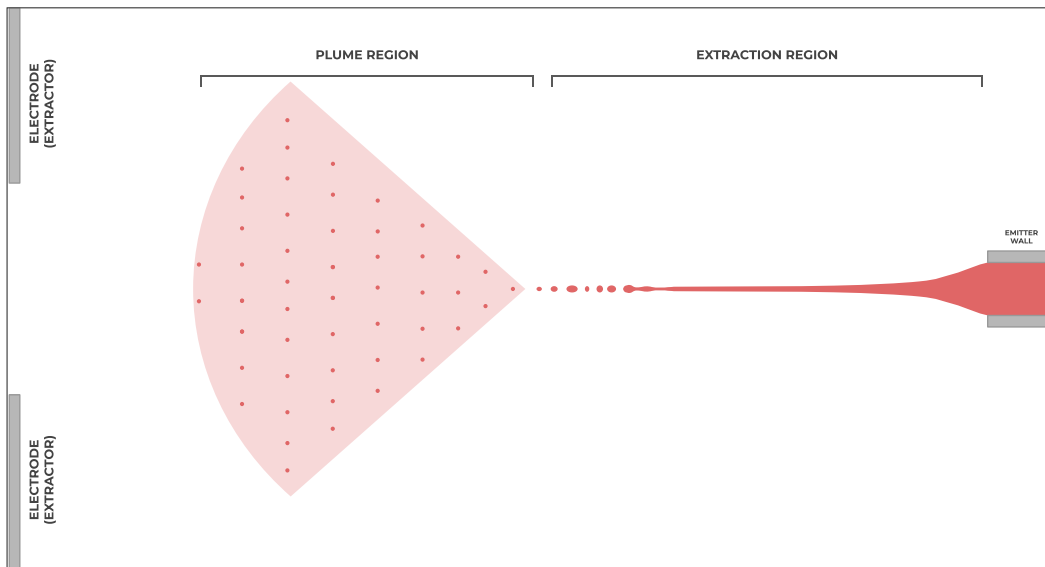
Fig. 1 Graphical representation of a typical electrospray setup.

The size of droplets formed during electrospray is influenced by various factors and operating parameters, including the liquid flow rate, applied voltage, liquid properties, geometry of the emitter, and finally the testing environment that this flow is produced in. The formation of small droplets is favored at higher voltages and lower liquid flow rates, allowing for a degree of control over the size distribution. This control is particularly advantageous in applications such as mass spectrometry, where precise droplet size is critical for accurate ionization and analysis. Similarly, high levels of control of electrospray operation benefit applications such as electric propulsion, as it provides a highly predictable behavior for attitude control in space. Additionally, the choice of liquid used in an electrospray device is pivotal for its proper operation. Commonly employed liquids include volatile solvents, ionic liquids, and even biological solutions. The selection depends on factors such as viscosity, conductivity, permittivity, and volatility. Ionic liquids, for instance, have gained prominence due to their low volatility, allowing for prolonged propulsion in space applications.

An intriguing aspect of electrospray phenomena is the ability to manipulate the charge on the droplets. The charge is typically imparted through ionization of the liquid. The nature of the solvent and the presence of dissolved ions influence the ionization process. The resulting charged droplets can be positively or negatively charged, depending on the nature of the ions involved. This charge manipulation plays a crucial role in the propulsion capabilities of electrospray thrusters. In the context of space propulsion, electrospray thruster devices have gained popularity as an enabling technology for the small satellite field. The ability to provide precise attitude control, in addition to the efficiency achieved through their high specific impulse, has sparked a myriad of new possibilities that tackle many of the challenges of the satellite industry. These devices are mainly used in low thrust applications, such as spacecraft precision control (orbital insertion, maneuvering, maintenance, etc.). In order to create enough thrust to propel a small spacecraft, these electrospray devices require strategic group positioning of multiple emitters. This arrangement of emitter is usually referred in literature as "multiplexing" [6,7].
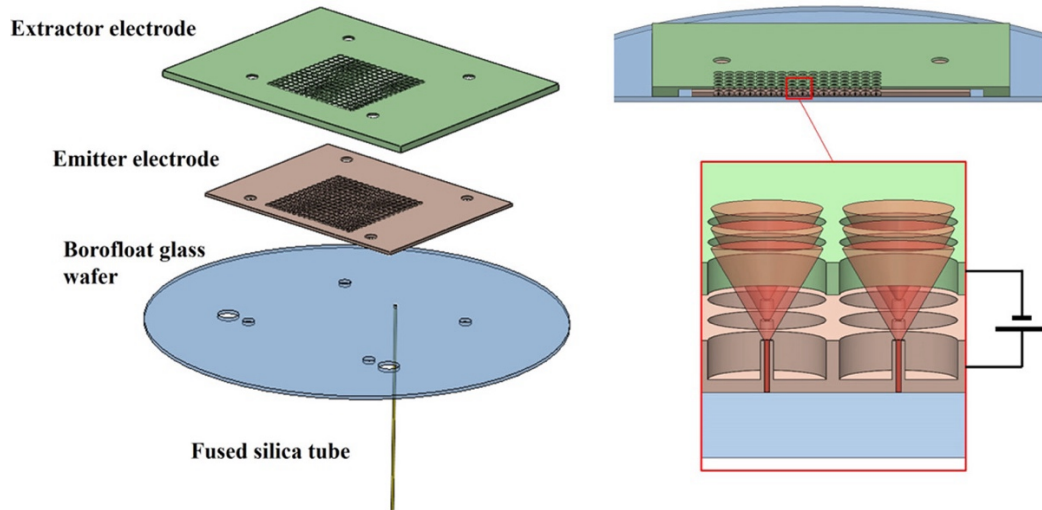
Fig. 2 Example of "multiplexed" emitter array of electrospray thrusters fabricated with advanced microfabrication techniques [8].

Furthermore, the scale of electrospray devices has allowed for the micro-manufacturing of propulsion systems, providing new alternatives for the miniaturization of spacecraft [8]. An example of a multiplexed electrospray system fabricated with microfabrication techniques is pictured in Fig. 2.

These thrusters are also characterized by their lack of complex dynamic parts and ease of operation, making it an ideal propulsion system for extended space missions. The efficiency of electrospray thrusters is further enhanced by their low power requirements. The electric field, responsible for the propulsion, demands relatively modest power inputs, aligning with the energy constraints often encountered in space applications. This characteristic contributes to the overall appeal of electrospray propulsion systems in the design of efficient and long-lasting satellite missions. In comparison to other electric propulsion alternatives, electrospray thruster provides outstanding power economy advantages due to their scalability. For example, ion engines, another form of electric propulsion, lack the flexibility to be downscaled to accommodate the power requirements of smaller satellites given their inherent power demands [9].

Despite the promising characteristics of electrospray thrusters, challenges persist. One significant hurdle involves the potential for electrode impingement and contamination [10]. The interaction of the liquid propellant with the emitter can lead to material degradation over time, impacting the thruster's

3

performance. Researchers are actively exploring materials and coatings to mitigate these challenges and enhance the durability of electrospray thrusters [6,10,11].

As with other complex fluid dynamic problems, an important tool used to understand and optimize fluid problems is advanced numerical simulations. These types of simulations allow for accurate prediction and analysis of electrospray behavior under varying operating parameters, while providing complementary value to experimentation. In some cases, experimentation may come at a high cost, as it is in the case of electrospray for propulsion purposes. In this scenario, numerical methods provide valuable insights for further design optimization. For this reason, this work deals with the adaptation of a numerical solver capable of proficiently simulating electrohydrodynamic phenomena. More specifically, an emphasis on electrospray processes has been given to the analysis presented.

II. Historical Background

Electrohydrodynamics is a field that has been long studied. In fact, it dates back to the late 1800's, when Rayleigh developed the first linear stability analysis of a droplet under an electric field [5]. In 1964, Taylor first delved into the conditions that would lead to cone formation, also known as the "Taylor Cone" [4]. In this work, Taylor proved that a liquid meniscus of conical shape could reach an equilibrium state when subjected to an electric field. This contribution also led to the discovery that this type of conical meniscus could only exist at semi-cone angle of 49.3°. Although Taylor was the first person to characterize the behavior of electrospray phenomena, there is an argument to be made regarding the systematic analysis of similar phenomena much earlier than Taylor [12]. In fact, in 1917, John Zeleny had arguably examined electrospraying behavior without fully characterizing it as such [13]. While he was unable to provide a theoretical explanation for this phenomenon, Zeleny's analysis has served as a basis for onset properties used in Taylor cone-jet emission [13].

a)   b)
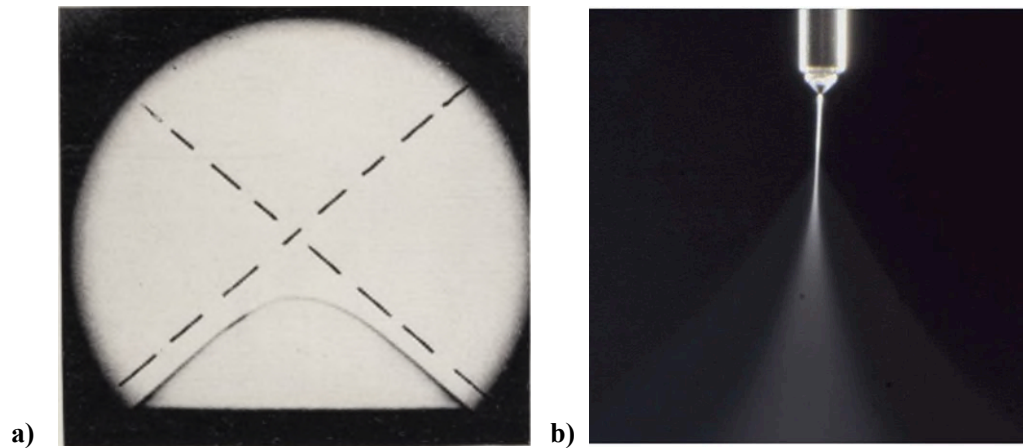
Fig. 3 a) Photography of cone formation a soap solution at equilibrium showing the semi-vertical angle discovered by Taylor [4]. Used with permission of The Royal Society (U.K.) from *Disintegration of Water Drops in an Electric Field by S.G. Taylor;* **permission conveyed through Copyright Clearance Center, Inc. b) Electrospray of ethanol in the steady cone-jet mode [14].**

In 1969, Melcher and Taylor presented the leaky dielectric model, a model that introduced a complete derivation of the governing equations related to the coupling of fluid dynamics and electrostatics [15]. This model makes several approximations that allow for simplifications of the equations of electromagnetism, reducing them to an electrostatic state. The assumption of characteristic time of magnetic phenomena being several orders of magnitude smaller than that of electric phenomena is what makes this simplification possible.

In recent years, most of the research in the field has focused on numerical simulations of this type of phenomena. With the existing complexity in replicating electrohydrodynamic phenomena in an experimental setting, numerical approaches often offer an insightful and feasible option to model electrospray phenomena. For this reason, several studies have emerged more recently.

In 2006, Lastow and Balachandran used the commercially available software ANSYS CFX 4.4 to simulate electrohydrodynamic atomization, in which they modified the existing heat conduction equation to solve the coupled EHD equations [16]. Due to the absence of the charge conservation method implementation, Lastow and Balachandran's model was unable to correctly represent the charge density inside the liquid bulk.

Using the leaky dielectric model proposed by Taylor and Melcher as a foundation, López-Herrera et al. introduced a charge-conservative approach for multiphase problems using the Finite Volume Method (FVM) software Gerris [17]. In comparison to other approaches, the FVM, when coupled with interface tracking methods, is capable of successfully capturing cone-jet formation as well as further droplet breakup. Other capabilities of this method include the ability to reproduce droplet deformation under the effects of an electric field. In 2013, Wei et al. developed a transient, multiphase solver that utilized a 2D axisymmetric framework to simulate the cone-jet mode. Similar to previous numerical approaches, Wei's work solved the electrostatic equations using the leaky dielectric model [18]. A couple of years later, Roghair et al. developed an FVM-based electrohydrodynamics model that was capable of correctly simulating fluid-fluid interfaces under an electric field. In their analysis, they successfully developed a multi-region numerical technique to simulate the deformation of interfaces for electrohydrodynamic problems. Rahmanpour and

Ebrahimi used ANSYS FLUENT to determine the shape of the cone jet. In their numerical study, no assumptions were made regarding initial shape and charge distribution of the cone-jet [19]. More recently, Dastourani et al. and Huh et al. have extended Roghair's work to simulate electrospray with liquids of low and high conductivities [20,21].
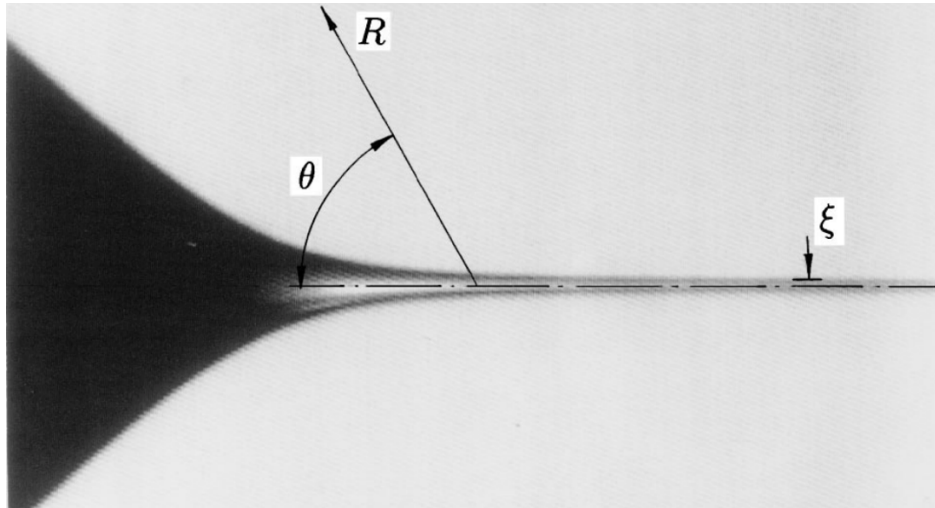
Fig. 4 Steady-cone jet photography obtained by Gañán-Calvo [22].

III. Governing Equations

A. Electrospray Phenomena

Electrospray phenomena represent a captivating and intricate realm within the domain of electrohydrodynamics, incorporating several topics that are associated with the disintegration of liquid into fine droplets under the influence of strong electric fields. As discussed in the introduction, the underlying principles of electrospray phenomena involve the application of high electric potentials to a liquid, often emerging from a capillary, leading to the formation of a Taylor cone and subsequent ejection of charged droplets. The interaction between electric forces, surface tension, and the fluid properties of the ejected liquid intricately governs the resulting droplet size, velocity, and overall jet behavior. The complex interdependence of these factors forms the foundation for diverse applications, including the controlled fabrication of nanoparticles, drug delivery systems, and advancements in mass spectrometry. In this section, an emphasis on physical parameters and governing equations that characterize electrospray phenomena will be given, with the purpose of elucidating its fundamental importance to the field of electric propulsion.

From an operational standpoint, there is a known range of operating parameters that allow for the formation of stable cone-jets. The stable cone-jet mode has gained relevance due to its direct application to nanoparticle generation, ion beam processes, and electrospray thrusters [23]. More importantly, the ability to control the initial diameter of the electrospray jet has proved to be an advantage for the cone-jet mode as it produces droplets that can be smaller than those emitted by other jet breakup phenomena, such as pressure atomizers. This initial diameter can be determined by the properties of the liquid chosen as the propellant. These properties include fluid properties such as electrical conductivity, permittivity, as well as operating parameters such as liquid flow rate and voltage applied. It is known, that for a given set of parameters (i.e. applied voltage and liquid properties), there is a range of liquid flow rates that would allow for the formation of a steady cone-jet. This range consists of a maximum and minimum flow rate value at which the cone-jet behavior becomes unstable. Equivalently, for a set of given flow rate and liquid properties, there is a range of applied voltages for which a steady cone-jet exists. A steady-cone jet is known as the emission that

remains in stable shape over a distance comparably longer than its jet diameter. A picture of a steady-cone jet is displayed in Fig. 5. The jet may reach a point of instability when it breaks up into many smaller droplets due to Rayleigh instabilities [5,24].
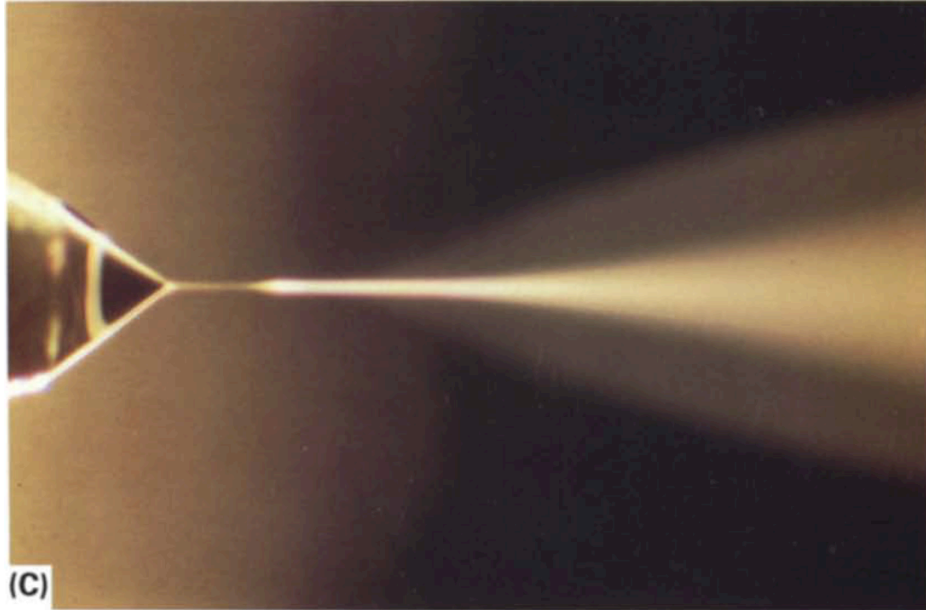
Fig. 5 A steady cone-jet of methanol ($\sigma = 4.5 \times 10^{-3} \, S/m$) with a small amount of hydrochloric acid [25]. Reprinted from "Zeroth-order, electrohydrostatic solution for electrospraying in cone-jet mode" by C. Pantano, A.M. Gañán-Calvo, A. Barrero, Copyright (1994), with permission from Elsevier.

An example of a stability parameter is the onset voltage, ϕ_{min}. The onset voltage is defined as the minimum electric potential that is required to achieve a hydrostatic cone. When a strong electric field is applied, the fluid at the emitter of an electrospray device will begin to deform due to the overcoming of the surface tension forces. Once the deformation begins, the electric field intensity at the tip of the fluid will continue to increase until all parts of the fluid surface tension forces reach an equilibrium with the electrostatic forces. When this equilibrium is reached, a cone measuring a half angle of 49.3 degrees is formed. The expression that defines this onset voltage is shown in Eq. 1. In this expression, r_e stands for

the radius of emitter, γ is the surface tension coefficient, and L_e is the distance from the emitter to the top electrode (extractor).

$$\phi_{min} = \sqrt{\frac{r_e \gamma}{\varepsilon_0}} \ln\left(\frac{2L_e}{r_e}\right) \tag{1}$$

Comparably, a relation for the minimum liquid flow rate exists in the form of Eq. 2, where ρ is the density of the liquid [20,26]. From this expression, it is clear that the minimum liquid flow rate is dependent on the fluid properties. It is crucial to highlight that this empirical expression is only valid for liquids with conductivities greater than $\sigma > 10^{-4} \, S/m$. As seen experimentally, the liquid flow rate has a direct impact on the diameter of the jet. Namely, in the cone-jet mode, the jet diameter decreases as the liquid flow rate decreases, causing the size of the droplet that originate from breakup to decrease as well [27]. When the value of the selected flow rate is significantly higher than Q_{min}, the hydrodynamic stresses become more prominent in the force equilibrium and a fully hydrodynamic jet takes place, instead of a cone-jet [28].

$$Q_{min} = \frac{\gamma \varepsilon}{\rho \sigma} \tag{2}$$

The comprehensive exploration of electrospray phenomena presented in this subsection underscores the crucial role that operating parameters play in shaping the intricate dynamics of this electrohydrodynamic process. Recognizing the paramount importance of these operating parameters not only enhances the fundamental understanding of electrospray phenomena but also provides a roadmap for optimizing and tailoring this process across a spectrum of applications.

B. Fluid Dynamics

The fluid dynamics involved in the present work are modeled using the incompressible Navier-Stokes equations. To track fluid quantities at the interface, this work uses a modified phase-fraction based interface capturing approach. This approach is commonly known as the Volume of Fluid (VOF) method. The volume of fluid introduces a tracking parameter, α, that allows for the solver to describe the interface

between multiple fluids [29]. This volume fraction parameter ranges from 0 to 1, usually indicating what fluid is present in each cell (i.e. $\alpha = 1$ indicates a cell full of fluid 1, while $\alpha = 0$ indicates a cell filled with fluid 2).

1. *Interface Tracking Method (Modified Volume of Fluid)*

By its strict definition, the Volume of Fluid (VOF) method is a computational technique widely employed in Computational Fluid Dynamics (CFD) to model and simulate fluid flows with distinct interfaces and free surfaces. Introduced by Hirt and Nichols in the 1980s [29], the VOF method tracks the volume fraction of each fluid phase within computational cells, allowing for the accurate representation of complex fluid interactions. The key concept involves solving a transport equation for the volume fraction, denoting the ratio of the volume occupied by one fluid phase to the total volume in a given computational cell. In its conventional sense, this approach enables the identification and tracking of fluid interfaces by using a threshold value for the volume fraction, making it particularly well-suited for problems involving multiple phases or fluid-fluid interactions.

When employing the interface tracking method for a two-phase flow, the VOF model treats two immiscible fluids as a unified effective fluid throughout the entire computational domain. Consequently, physical properties of this fluid, such as density and viscosity, can be determined through the computation of a weighted average of the volume fraction, as it can be seen from Eq. 5 and 6. Regarding the solution of the volume fraction, the transport equations are solved alongside the Navier-Stokes equations. The transport equation for the volume fraction is given by Eq. 3 and can be defined as the conservation of the mixture components along the path of a fluid parcel.

In the traditional VOF, the volume fraction field is solved at each time step according to Eq. 3.

$$\frac{\partial \alpha}{\partial t} + \nabla \cdot (\alpha \vec{u}) = 0 \tag{3}$$

A modified version of the VOF method was proposed by Ubbink and Issa in their interface compression algorithm [30]. The purpose of this implementation is to counteract numerical diffusion at the

11

interface by adding an artificial compression term to Eq. 3. With the addition of this term, the expression now takes on the following form, where $\vec{u}_c$ is the artificial compression velocity [31]. In physical terms, this velocity can be explained as the relative velocity between the two present fluids, stemming from variations in density and viscosity across the fluid-fluid interface.

$$\frac{\partial \alpha}{\partial t} + \nabla \cdot (\alpha \vec{u}) = \nabla \cdot [(\alpha - \alpha^2)\, \vec{u}_c] \tag{4}$$

In the fluid flow, the density and viscosity variables are assigned to each computational cell using a weighted arithmetic averaging method.

$$\rho = \rho_1 \alpha + \rho_2 (1 - \alpha) \tag{5}$$

$$\mu = \mu_1 \alpha + \mu_2 (1 - \alpha) \tag{6}$$

The surface tension source term is calculated using the Continuum Surface Force (CSF) approach developed by Brackbill et al. [32]. In this model, the surface tension force is distributed volumetrically, and it is only present in the computational cells that contain parts of the fluid-fluid interface. The CSF approach models the surface tension force as follows:

$$F_\gamma = \gamma \kappa (\nabla \alpha) \tag{7}$$

Where γ represents the surface tension coefficient and κ is the curvature of the interface. This interface curvature, which is the opposite of the divergence of the unit normal vector, $\hat{n}$:

$$\kappa = -\nabla \cdot \hat{n} = \nabla \cdot \left(\frac{\nabla \alpha}{|\nabla \alpha|}\right) \tag{8}$$

In Eq. 8, α refers to the volume fraction used in the VOF model.

The continuity and momentum equations used in the model are given by the Navier-Stokes equations and are represented below.

$$\nabla \cdot \vec{u} = 0 \tag{9}$$

$$\rho\left(\frac{\partial\vec{u}}{\partial t} + \vec{u} \cdot \nabla\vec{u}\right) = -\nabla p + \nabla \cdot \left[\mu\left(\nabla\vec{u} + \nabla\vec{v}^{\mathrm{T}}\right)\right] + \rho\vec{g} + \vec{F}_\gamma + \vec{F}_{ES} \tag{10}$$

In Eq. 9 and 10, $\vec{u}$ is the velocity vector. ρ denotes the fluid density, $\vec{g}$ is the gravity vector and p is the pressure. The term $\vec{F}_\gamma$ describes the forces due to surface tension. $\vec{F}_{ES}$ is the body force acting on the fluid as a result of the presence of the electric field, $\vec{E}$.

With the derivation of the Maxwell Equations applicable to electrostatics, it is possible to couple the electrostatic forces to the fluid interface. An in-depth description of the electrostatics involved in this study is given in the next subsection. The electric force $\vec{F}_{ES}$ is what allows us to couple the equations of fluid motion by adding it as a body force to the momentum equation listed in Eq. 10. This can be done using the electrostatic Maxwell stress tensor. The definition of the electrostatic Maxwell Stress Tensor is given in Eq. 11, where $\vec{\vec{I}}$ is the identity matrix. The electrostatic force is then defined as the divergence of the Maxwell Stress Tensor.

$$\vec{\vec{T}}_{MST} = \varepsilon_0\vec{E}\vec{E} - \frac{1}{2}\varepsilon_0\left(\vec{E} \cdot \vec{E}\right)\vec{\vec{I}} \tag{11}$$

$$\vec{F}_{ES} = \nabla \cdot \vec{\vec{T}}_{MST} \tag{12}$$

C. Electrostatics

In order to calculate $\vec{F}_{ES}$ and couple the electric forces with the fluid dynamics effects involved in electrospray phenomena, we must start with Maxwell's equations of electromagnetism.

$$\nabla \times \vec{E} + \frac{\partial\vec{B}}{\partial t} = 0 \tag{13}$$

$$\nabla \times \vec{H} - \frac{\partial\vec{D}}{\partial t} = \vec{J} \tag{14}$$

$$\nabla \cdot \vec{D} = \rho_E \tag{15}$$

$$\nabla \cdot \vec{B} = 0 \tag{16}$$

Here, Eq. 13-16 refer to Faraday's Law of Induction, Ampere's Law, Gauss's Law of Electricity, and Gauss's Law of Magnetism, respectively. In these differential equations, $\vec{E}$ is the electric field intensity vector, while $\vec{B}$, $\vec{D}$, $\vec{H}$, and $\vec{J}$ are defined as the magnetic field flux, the electric displacement field, the magnetic field intensity, and the electric current density, respectively. ρ_E stands for the charge density.

D. Leaky Dielectric Model for Electrostatics

In the context of electrohydrodynamics, the leaky dielectric model developed by Melcher and Taylor is particularly relevant for understanding and predicting the behavior of liquids in the presence of electric fields [15,33]. This model treats both fluids as ohmic conductors, in which a charge leakage through the liquid is allowed. The understanding of poorly conducting liquid, known as "leaky dielectrics" began with the studies performed by Allan & Mason in 1962 [34]. In their work, they delved into the conditions under which liquid drops could burst, shedding light on the mechanisms involved in the breakup of fluid particles.

In the original derivation of the leaky dielectric model, charge convection is neglected, leading to a natural decoupling of the physics involved in electrohydrodynamics (electrostatics and fluid dynamics) [35]. This approach fails to model ionic concentration dynamics, which, under strong electric fields, are arguably indispensable in successfully replicating the behavior of electrohydrodyamic phenomena [36–38].

In summary, the leaky dielectric model provides a comprehensive framework for understanding the behavior of droplets deformed by electric fields, and experimental studies have demonstrated qualitative and quantitative agreement with the model. The model proposed by Melcher and Taylor serves as the precursor for the charge conservative approach implemented in this work.

Due to the characteristic time for electric phenomena, $t_e \approx \frac{\varepsilon}{\sigma}$, being orders of magnitude greater than that of magnetic phenomena, $t_m \approx \mu_m \sigma \ell^2$, a further simplification on the Maxwell's equations can be made. In these expressions, ε is defined as $\varepsilon = \varepsilon_r \varepsilon_0$. Here, ε_r and ε_0 are the relative permittivity and the permittivity of vacuum, respectively. σ refers to the liquid electric conductivity, while μ_m and ℓ refer to the magnetic permeability and the characteristic length, respectively.

According to Saville, the leaky dielectric model allows for the neglection of magnetic effects. Under static conditions, such as the ones employed in electrospray devices, electric and magnetic effects are independent of each other because their fields are not coupled [39].

Considering only electrostatics ($\vec{B} = \vec{H} = 0$), Eq. 13 becomes

$$\nabla \times \vec{E} = 0 \tag{17}$$

Since $\vec{E}$ is irrotational, it can also be written as the gradient of the scalar potential field:

$$\vec{E} = -\nabla \phi \tag{18}$$

where ϕ denotes the electric potential. Taking the divergence of Ampere's Law (Eq. 14) and using the vector identity $\nabla \cdot \nabla \times \vec{A} = 0$ (where $\vec{A}$ is any vector) yields:

$$\nabla \cdot \left[\nabla \times \vec{H} \right] - \nabla \cdot \frac{\partial \vec{D}}{\partial t} = \nabla \cdot \vec{J} \tag{19}$$

$$-\frac{\partial}{\partial t} \left(\nabla \cdot \vec{D} \right) = \nabla \cdot \vec{J} \tag{20}$$

Then, using Gauss's Law for Electricity (Eq. 15) yields the following expression.

$$\frac{\partial \rho_E}{\partial t} + \nabla \cdot \vec{J} = 0, \tag{21}$$

the current density vector $\vec{J}$, can be represented as

$$\vec{J} = \sigma \vec{E} + \rho_E \vec{u} \tag{22}$$

Here, the current density is given by the sum of the conduction and convection current density. The conduction current density term, $\sigma\vec{E}$, is also known as the point form of Ohm's law. Combining Eq. 18 and 22 into Eq. 21 yields the charge conservation equation:

$$-\frac{\partial \rho_E}{\partial t} = \nabla \cdot [-\sigma\nabla\phi + \rho_E\vec{u}] \tag{23}$$

The first term on the right-hand side of the equation is known as the charge conduction term, while the second term is known as the charge convection term [17].

To solve for the electric field, Gauss's Law for electricity (Eq. 15) is utilized. Assuming the ambient fluid is homogenous and isotropic allows for the electric displacement $\vec{D}$ to be defined as the product of electrical permittivity and the electric field intensity. Using Eq. 18 allows for the derivation of the Poisson equation that relates the electrostatic field with the free electric charges in the domain.

$$\vec{D} = \varepsilon\vec{E} \tag{24}$$

$$\nabla^2\phi = -\frac{\rho_E}{\varepsilon} \tag{25}$$

In domains where multiple fluid phases are present, an averaging method is required to calculate properties in interfacial cells. To determine the average conductivity and permittivity in each cell, an averaging parameter based on the work by Huh [21] is used here:

$$\sigma = \left[\sigma_1^{1/f}\alpha_1 + \sigma_2^{1/f}(1-\alpha_1)\right]^f \tag{26}$$

$$\varepsilon = \left[\varepsilon_1^{1/f}\alpha_1 + \varepsilon_2^{1/f}(1-\alpha_1)\right]^f \tag{27}$$

The averaging parameter, f, allows for the expressions below to reduce to the Weighted Arithmetic Mean (WAM) method when $f = 1$, and the Weighted Harmonic Mean (WHM) when $f = -1$. The WAM has been implemented in several relevant numerical EHD studies [17,18,20,40,41], but has struggled to appropriately treat mass conservation and electric charge at the fluid-fluid interface. For this reason, and based on the suggestions made by Huh et al., adding this cell-averaging scheme allows for greater control of droplet size and charge conservation for fluids like heptane.

IV. Numerical Approach

A. Multiphase Flow Solver (InterFoam)

In this present work, a numerical approach using a multiphase method in the open-source CFD Software, OpenFOAM, is proposed [42,43]. OpenFOAM takes advantage of the Volume of Fluid (VOF) approach to track fluid interfaces [44]. The interFoam solver has been modified to include the coupling of electrostatic forces with existing fluid dynamics while making no simplifications of the charge conservation method. OpenFOAM provides the significant advantage of allowing users to make modifications to the existing fluid dynamics algorithm. In comparison to the leaky dielectric model, the modified solver presented in this work includes the charge conservation equation approach based on López-Herrera's work [17]. Here, the time derivative term in the charge conservation equation is preserved. An in-depth explanation of this method was presented in Section III.

For the solution of the Navier-Stokes equations, the PIMPLE algorithm is employed. The PIMPLE algorithm is a key computational tool within the OpenFOAM platform, designed to address the challenges inherent in transient fluid flow simulations [45]. This algorithm combines the strengths of the PISO (Pressure-Implicit Split Operator) and SIMPLE (Semi-Implicit Method of Pressure-Linked Equations) algorithms, creating a synergistic approach for solving unsteady flow problems. Operating through a cyclic process, PIMPLE alternates between explicit and implicit phases within each time step. The explicit phase employs the PISO algorithm to iteratively update the velocity field, providing stability and accuracy in capturing transient phenomena. Subsequently, the implicit phase refines the pressure field using the SIMPLE algorithm, ensuring consistency and convergence. The SIMPLE algorithm is commonly used for steady-state analysis, while the PISO algorithm is capable of dealing with transient calculations. The integration of these two well-established methodologies enables PIMPLE to deliver robust performance across a diverse range of fluid dynamics scenarios. The implementation of the PIMPLE algorithm allows the user to reach solution convergence by adding outer correctors to ensure that the explicit components of

17

any partial differential equation are converged. A general description of the algorithm used to solve the discretization of these equations is pictured in Fig. 7. Under this algorithm, there are several requirements needed to achieve stability and convergence of the solution. Most importantly, the solver tolerance for each of the discretized equations must be lower than the residual tolerance set for the PIMPLE method. Then, for added stability, under-relaxation factors can be used. However, the use of under-relaxation factors can slow down the convergence rate, and consequentially, increase the run time of a given simulation. To analyze convergence, a quantity of interest, such as the velocity magnitude or the volume fraction averaged over the whole domain is evaluated over time.

1. MEPSFoam Solver

The adapted solver in this work, namely the MEPSFoam (**M**ultiphase **E**lectrohydrodynamic **P**henomena **S**olver), is a modified version of the original interFoam solver that is already included in the open-source CFD software, OpenFOAM. This multiphase solver has been revised to include effects due to electrostatic forces in the fluid-fluid interface. A comprehensive review of the capabilities of the base interFoam solver and its performance has been carried out by Deshpande et al. [44]. In their evaluation, the authors concluded that interFoam's performance is comparable to other VOF solvers. Specifically for surface tension-dominated flows, Deshpande showed that its capabilities are on par with multiphase solvers such as the one developed by Francois et al., which uses a face centered balanced force approach [46].

The major advantage of interFoam compared to other solvers is its accessibility. Due to its open-source availability, interFoam is easily accessible while also having the technical support of thousands of users around the world. Additionally, it is comfortably modifiable, making it the ideal toolkit for researchers looking to add further physical capabilities to an already rich solver.

18

2. Modifications to Solver

Compared to previous EHD solvers that have used OpenFOAM, such as those developed by Roghair and Huh [21,47], the MEPSFoam solver has been adapted using a much newer version (OpenFOAM Version 8), taking advantage of improved performance and robustness for multiphase problems. Examples of these improvements include the development of the selectable interpolation for interface-capturing capability as well as the new family of piecewise-linear interface calculation (PLIC) scheme [48]. Among other enhancements, a more efficient Crank-Nicolson numerical scheme has been added for second-order time discretization.

As part of the modifications made to the solver, dictionaries for electrostatic variables and fields were implemented into the base OpenFOAM 8 software. Specifically, dimensioned variables were introduced for the electric conductivity and electric permittivity. This addition allows for the user to specify the fluid properties for any given problem. Similarly, other fields such as the electric potential, charge density, and the tensor field for the Maxwell Stress Tensor were calculated.

In the same manner, an equation to solve for the electric field intensity has been introduced. An excerpt of the discretization of this equation, $\nabla^2 \phi = -\frac{\rho_E}{\varepsilon}$, (Eq. 25) is shown in Fig. 6.

```
// Calculate Poisson Eq.
 fvScalarMatrix PoissonEqn
        (
            fvm::laplacian(eps,elec_pot)== -rho_E
        );
        PoissonEqn.solve();

//Calculate the Electric Field using the gradient of the Electric Potential
        E = -fvc::grad(elec_pot);
        magE = mag(fvc::grad(elec_pot));
```

Fig. 6 OpenFOAM discretization of Eq. 25 to solve for charge Density, ρ_E and electric field intensity, E.

In order to solve for the electrostatic forces at the interface, the divergence of the Maxwell Stress Tensor $\vec{\vec{T}}_{MST}$ was discretized using the OpenFOAM equation discretization method [49]. To couple this force with the equations of fluid motion, the electrostatic force $\vec{F}_{ES}$ is included in the discretization of the

momentum equation in the MEPSFoam solver. In the original interFoam solver, the momentum equation is solved with no inclusion of the electrostatic force. The solver developed by Roghair et al. served as an initial guide to correctly implement the discretization of the electric equation in the PIMPLE algorithm [41,47].

Last but not least, the averaging procedure mentioned in Section III (Eq. 26 and 27) was inserted into the solver to describe the scalar values of the electrical conductivity and permittivity, and therefore, solve for the volume fraction at each computational cell.

3. Numerical Methods

For the time-discretization, the Crank-Nicolson scheme, a second-order accurate temporal scheme, was selected. As implemented, this scheme uses a blending factor, ψ, to blend between a pure Euler scheme ($\psi = 0$) and a pure Crank-Nicolson scheme ($\psi = 1$). A value of $\psi = 0.9$ is normally used for a compromise between accuracy and robustness. For spatial discretization, a Gauss upwind scheme is used for the divergence terms containing velocity and charge density variables. A smooth solver (Gauss-Seidel) is used to solve for the velocity and a pre-conditioned conjugate gradient solver for the pressure. The charge conservation equation is solved using a precondition bi-conjugate gradient linear solver as it is a widely known solver effective for asymmetric matrices.

The time step required for these simulations was calculated with two main constraints in mind. The first constraint considered was the characteristic time for electric phenomena, $t_e \approx \frac{\varepsilon}{\sigma}$, as it determines the relationship between the electric permittivity and conductivity of the conductive fluid. Additionally, to maintain stability in the solver, the time step chosen must be able to keep the maximum Courant number below the threshold selected ($Co = 0.5$). For this to be possible, the time step must obey the criterion, $Co_{max} < 0.5$, where Co is defined as follows:

$$Co = \sum_i \frac{U_i \Delta t}{\Delta L_i} \tag{28}$$

For multi-dimensional representations, the maximum Courant number is estimated as a sum of all dimensions. In Eq. 28, Δt is the time step, U is the velocity of the flow, and ΔL is the characteristic length of the mesh in each dimension. In order to satisfy this condition, an initial of $\Delta t = 2 \times 10^{-5}\ s$ is prescribed, while the adaptive time-stepping capability in the solver adjusts the time step to satisfy the criterion whenever needed. The time step required for most instances in time is in the order of $\Delta t = 1 \times 10^{-8}\ s$.
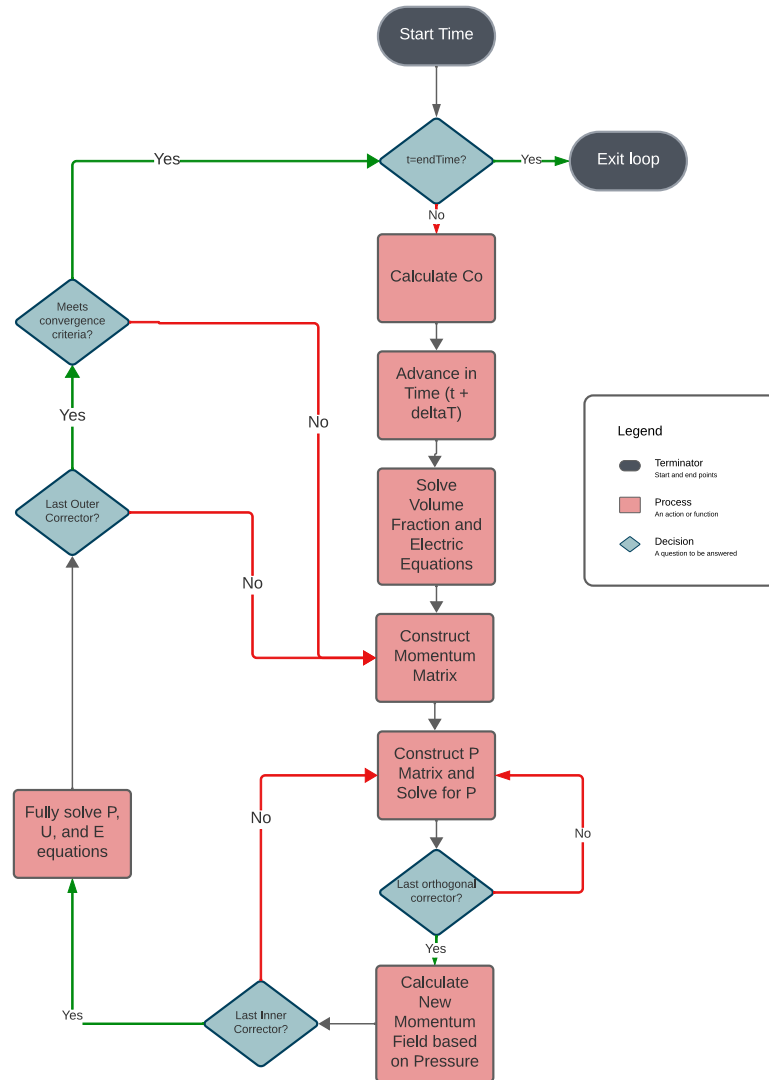
Fig. 7 Flowchart of MEPSFoam solver algorithm.

B. Validation

1. Fluid-Flow Benchmark: Rising Bubble in Liquid Column

To prove the validity of the solution of the Navier-Stokes after the coupling of the electric equations, a two-dimensional problem involving a rising bubble in a liquid column is considered [50]. In this problem, all electric effects have been neglected by setting the electric potential, electric permittivity, and electric conductivity to zero. The case consists of placing a circular bubble of radius r in a rectangular domain. The configuration used for this test case is shown in Fig. 8. As pictured in this figure, the circular bubble is placed at a location $(x = 0.5\ m, y = 0.5\ m)$. The initial radius of the bubble R_d is set to 0.25 m. The total physical duration of the simulation is 3 s. Two cases are considered to test the accuracy of the fluid solver compared to other numerical simulations that have been performed in recent years.
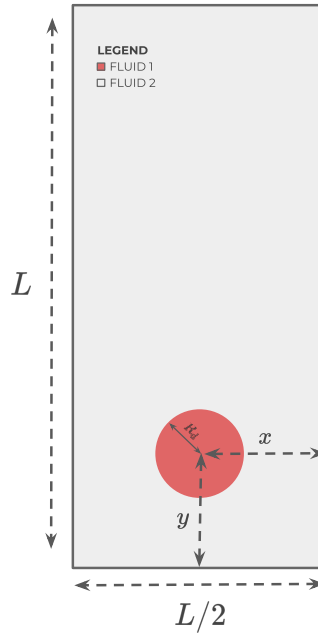
Fig. 8 Rising bubble geometry and problem setup.

Three main results are analyzed: Bubble geometry at $t = 3\ s$, mean rising velocity over time, and center of mass of the bubble. The parameters used in the two test cases are displayed in Table 1. In this table, the dimensionless number, Reynolds Number Re and the Eötvös Number Eo, are introduced. These dimensionless quantities are widely used to predict fluid flow patterns. The Reynolds Number is defined as $Re = \frac{\rho_1 u_g L_c}{\mu_1}$, where ρ_1 is the density of fluid 1, u_g is the gravitational speed, L_c is the characteristic length, and μ_1 is the dynamic viscosity of fluid 1. Here, $u_g = \sqrt{L_c g}$. The characteristic length is further described as $L_c = 2R_d$. By its strict definition, the Reynolds Number characterizes the interaction between inertial and viscous forces present in the fluid. Similarly, the Eötvös number, defined as $Eo = \frac{\rho_1 u^2 L_c}{\gamma}$, indicates the relationship between gravitational and surface tension forces.

Table 1 Parameters used in Rising Bubble Test Case

Test Case	Density, ρ_1 $\left(\frac{kg}{m^3}\right)$	Density, ρ_2 $\left(\frac{kg}{m^3}\right)$	Dynamic Viscosity, $\mu_1(Pa \cdot s)$	Dynamic Viscosity, $\mu_2(Pa \cdot s)$	Surface Tension Coefficient, $\gamma\left(\frac{N}{m}\right)$	Reynolds Number, Re	Eötvös Number, Eo
1	1000	100	10	1	24.5	35	10
2	1000	1	10	0.1	1.96	35	125

To quantify the results obtained using the MEPSFoam solver, they have been compared with benchmark data generated using the three different participating groups in Hysing et al. work [50]. The three groups mentioned in this study are as follows: TU Dortmund, EPFL Lausanne, and Uni Magdebug. TU Dortmund utilized the TP2D (Transport Phenomena in 2D) Code to solve this problem. This flow solver treats immiscible fluids using the level set method [51,52]. The second group, EPFL Lausanne, uses the Finite Element Method (FEM) software, FreeLIFE, designed to solve free-surface two-fluid problems. This solver adopts a level-set approach to capture the interface between the two fluids [53]. Thirdly, the Uni Magdebug participating group uses an incompressible two-phase flow solver that incorporates a

Lagrangian-Eulerian approach. This solver is named MooNMD and it stands for **M**athematics and **o**bject-oriented **N**umeric in **M**ag**D**eburg [54]. Similar to the previous two solvers, MooNMD adopts a FEM approach. It is important to note that all 3 solvers make use of a second-order time discretization scheme: one-step-theta, BF2, and fractional-step-theta, respectively.

To compare the shape of the bubble at $t = 3\ s$, the interface between the fluid 1 and fluid 2 has been characterized. This allows for an accurate representation of the geometrical shape of the bubble at the end of the simulation. To calculate the center of mass of the bubble, the following definition is employed:

$$X_{CoM} = (x_{CoM}, y_{CoM}) = \frac{\int_{A_b} x\ dx}{\int_{A_b} 1\ dx} \qquad (29)$$

Where, the region occupied by the bubble is denoted by A_b. In a similar manner, the rise velocity is defined as the average velocity at which the bubble or drop rising. This velocity is averaged over the entire computational domain and can be defined as:

$$U_{avg} = \frac{\int_{A_b} u\ dx}{\int_{A_b} 1\ dx} \qquad (30)$$

These quantities are represented in the figures below. In both cases, the MEPSFoam solver produces largely aligned results to those mentioned above. The second test case is considered a more challenging problem as it exposes the limitations of the different interface tracking methods at large density and viscosity ratios between the two fluids involved. Additionally, the occurrence of break up is partially responsible for the small discrepancies in the results.
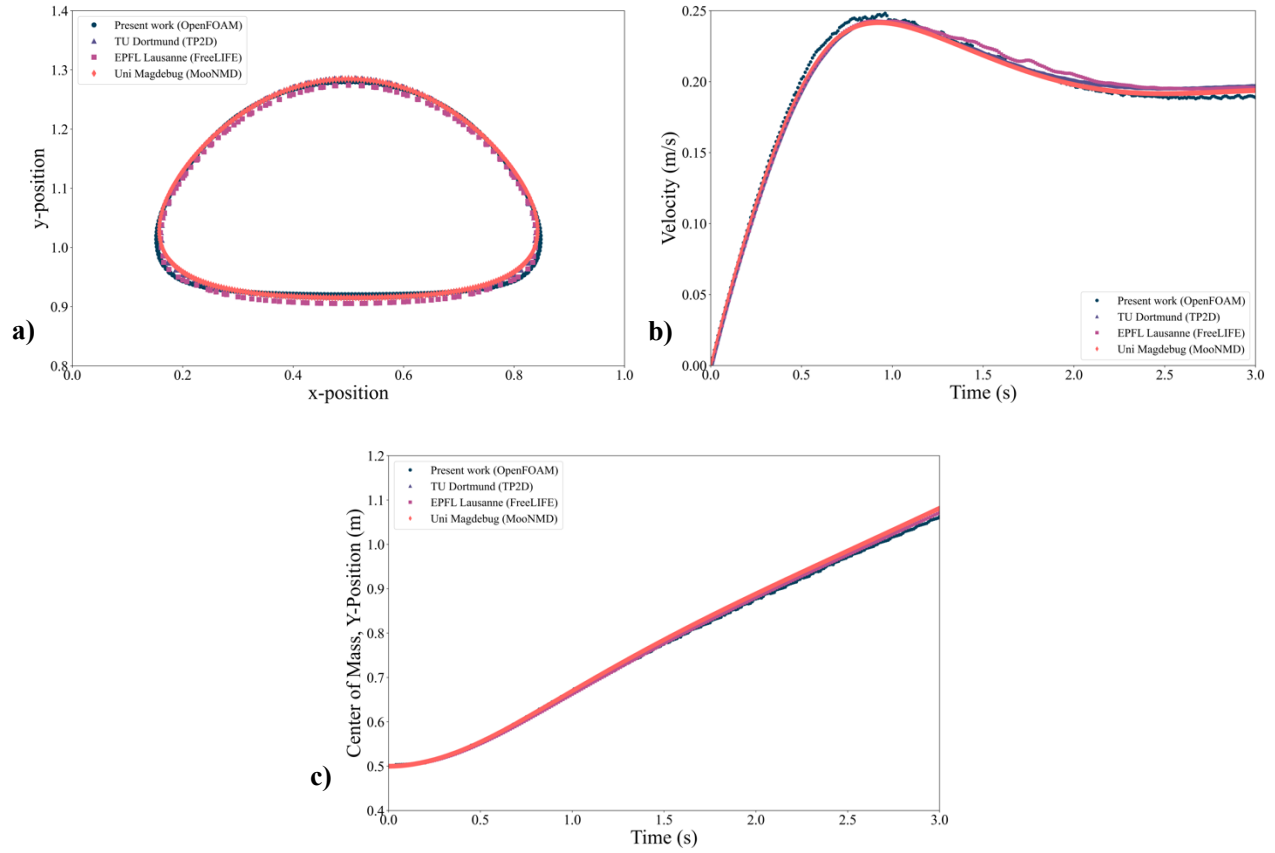
Fig. 9 Test case 1 results for MEPSFoam solver. a) Bubble geometry at $t = 3$ s. b) Bubble rise velocity over time. c) Center of mass calculation over time.
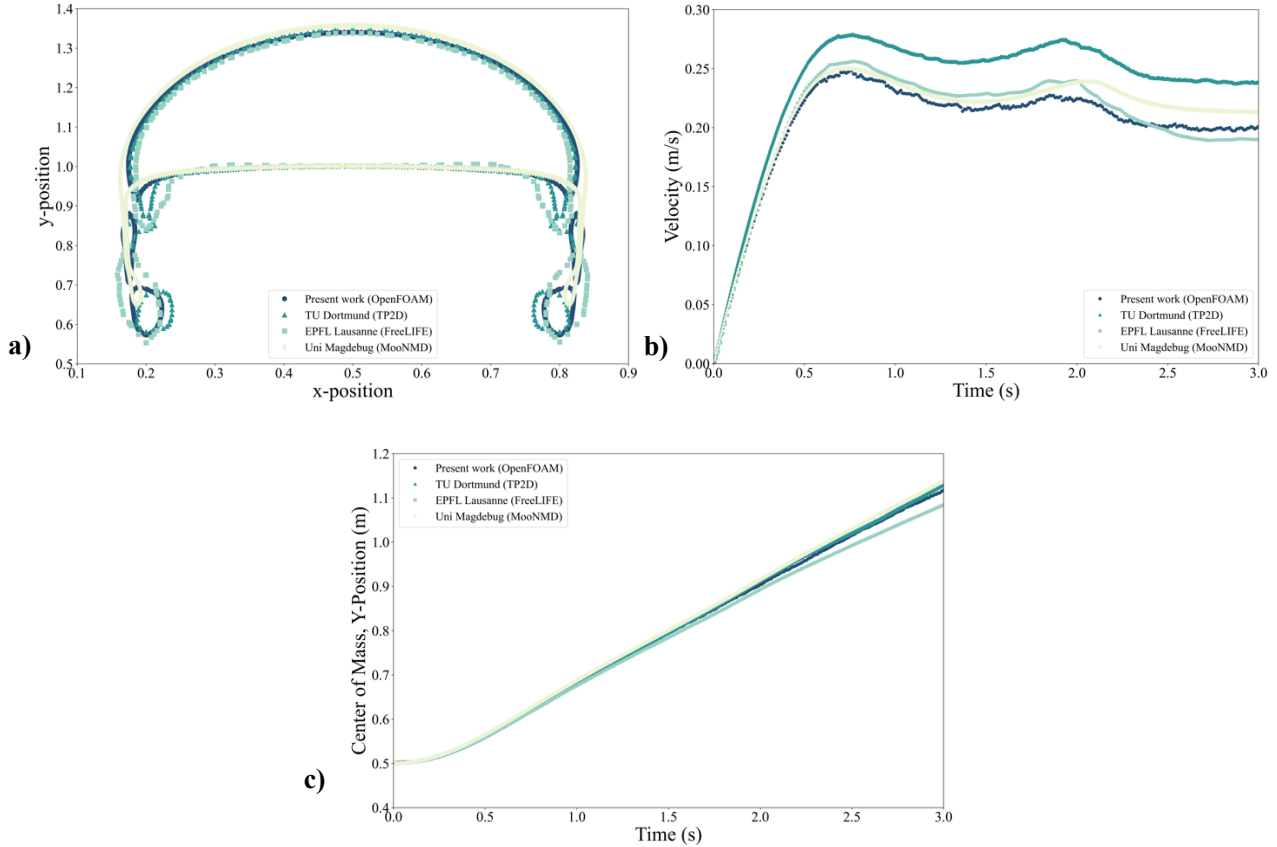
Fig. 10 Test case 2 results for MEPSFoam solver. a) Bubble geometry at $t = 3$ s. b) Bubble rise velocity over time. c) Center of mass calculation over time.

Qualitatively, it is possible to compare the two cases considered in this benchmarking scenario using the computed interface geometries with the diagram extracted from Clift et al [55]. For both test cases, the shapes obtained computationally appear to be in agreement with the plot below. As shown in and given the properties of both cases, the first test case models an ellipsoidal bubble, while the second one resembles a skirt-shaped bubble. In addition to its dimensionless properties, test case 2 also has a lower surface tension coefficient, meaning that the surface tension effects are not strong enough to hold the shape of the bubble together, allowing it to break up.
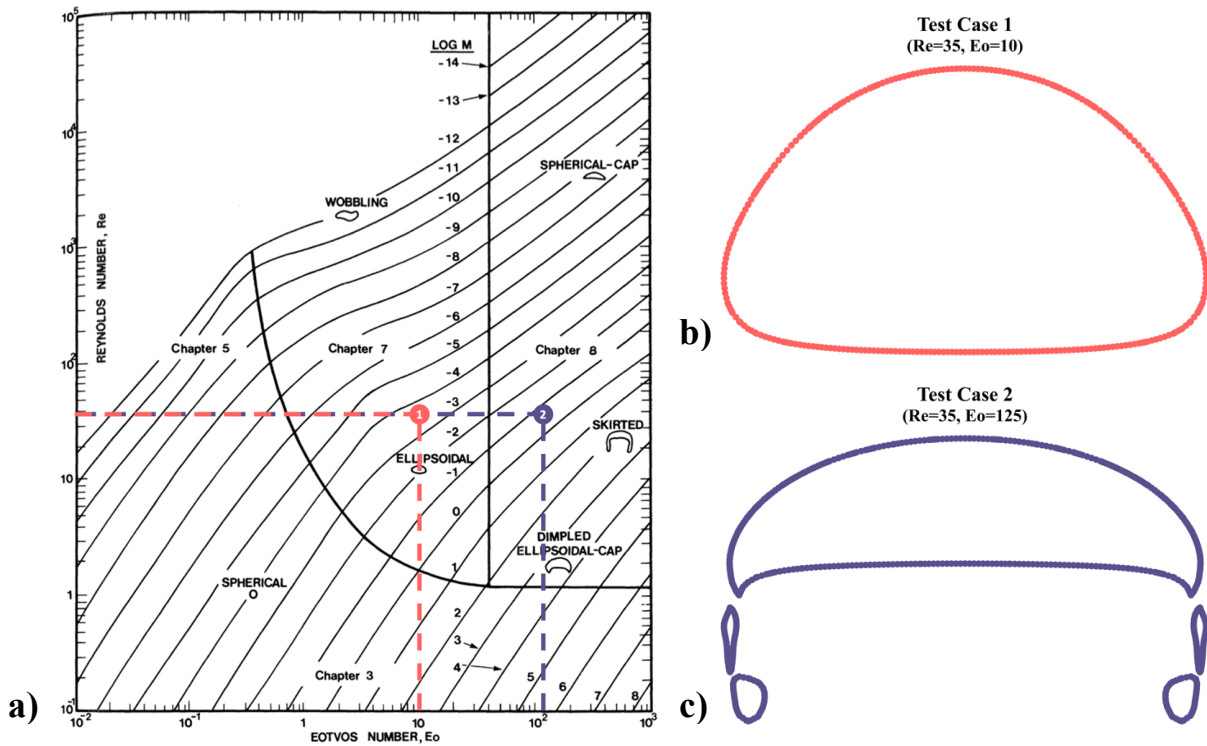
Fig. 11 Geometrical regimes for bubble/drops through a liquid column as function of *Re* and *Eo*. Diagram from Clift et al [55].

2. *Validation of the Solution of the Maxwell Equations with No Induced Flow*

To further validate the implementation of the Maxwell Equation while minimizing induced flow effects, two main cases are considered: a charge relaxation test case and conductive/dielectric planar layer test case.

Charge Relaxation/Decay

To verify the implementation of the charge-conservation approach, a test case consisting of a two-dimensional Gaussian charge bump is considered. The setup consists of a single, conducting liquid in a square domain of $L = 1\ m$. The electric potential, ϕ, is set to 0 at all boundaries. Similarly, no initial velocity has been introduced to the problem. Conductivity σ and permittivity ε were chosen to be $\sigma = 1\ S/m$ and $\varepsilon = 2\ F/m$. Gravitational effects have been neglected in this problem.

27

This test case has been inspired by the work of López-Herrera [17]. A uniform charge density profile at $t = 0\ s$ is initialized in a circular shape with radius a, using the Gaussian expression in Eq. 31.
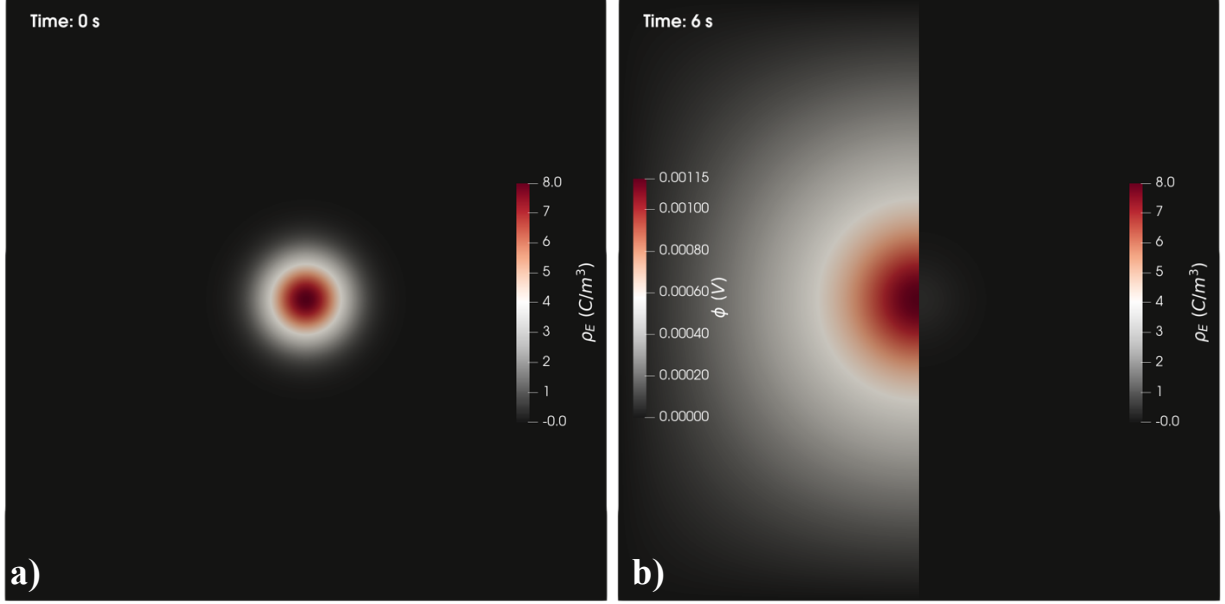
Fig. 12 Gaussian charge decay simulation. a) Initial gaussian charge density profile at $t = 0\ s$. b) Left, electric Potential at $t = 6\ s$. Right, charge density profile at $t = 6\ s$.

$$\rho_E(x, t = 0) = \frac{e^{\frac{-r^2}{2a^2}}}{a\sqrt{2\pi}} \tag{31}$$

Here, r is the radial coordinate, $r^2 = x^2 + y^2$, and a is selected to be $a = 0.05\ m$. The parameter a allows us to set the standard deviation of the Gaussian distribution. Under the assumption that the domains wall are several orders of magnitude further from the charge bump ($a \ll L$), the analytical solution simplifies to an exponential time charge decay (Eq. 32). As time proceeds in the simulation, it is observed that the charge accumulation in the domain begins to decay.

$$\rho_E(x, t) = e^{-\frac{\sigma t}{\varepsilon}} \tag{32}$$

Fig. 13 exhibits the charge relaxation behavior of the initial Gaussian distribution. The spatial distribution at different times is also shown. The plot in Fig. 14 shows the results obtained when using Eq. 31 with $x = y = 0$, meaning that the charge bump is initialized at the center of the computational domain.

28

In this figure, the maximum charge density as a function of time is illustrated. Numerical and analytical results show good agreement, indicating a successful implementation of the charge conservation equation and the effects of conductivity.
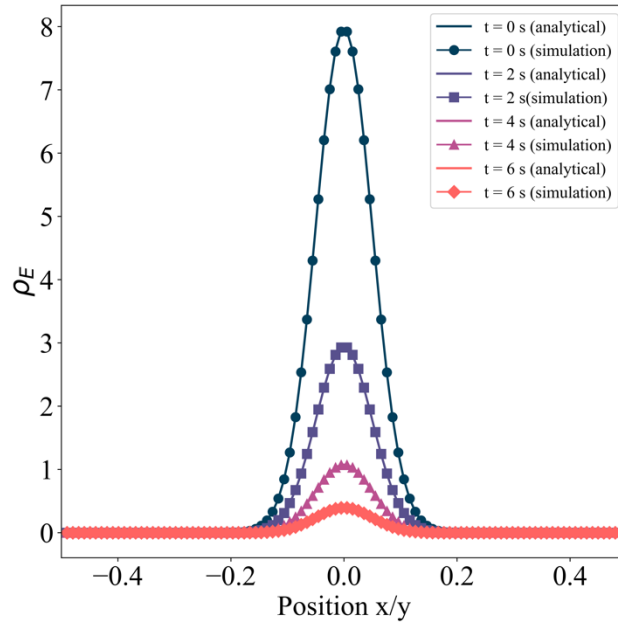
Fig. 13 Distribution of charge as a function of position at $t = 0, 2, 4, 6\ s$.
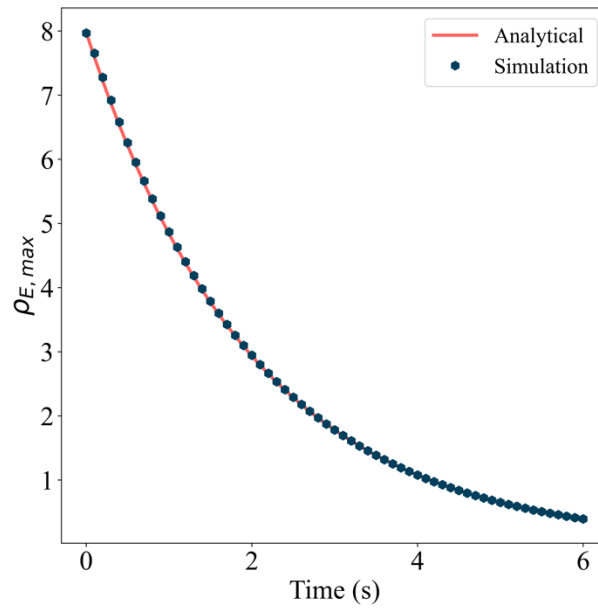
Fig. 14 Transient relaxation of maximum charge density at center of domain $(x = 0, y = 0)$.

Planar Layer Test Case

The second validation test, the Planar Layer test case, consists of setting a one-dimensional domain of $L = 1\,m$ with two vertically stacked liquids. This validation test provides proof of successful implementation of the solution of Eq. 25. Three different cases are considered for the Planar Layer test: two conducting liquids, two dielectric liquids ($\sigma_1 = \sigma_2 = 0\,S/m$), and one conductive liquid/one dielectric liquid ($\sigma_2 = 0$). The configuration for this validation case is depicted in Fig. 15. The parameters for these cases are shown in Table 3. Note that, since OpenFOAM is unable to use 0 for the entry of dielectric conductivities, are very small number has been used instead ($\sigma = 1 \times 10^{-50}\,S/m$).

For this configuration, the top wall is open to atmospheric conditions. Furthermore, a no-slip velocity boundary condition and voltage of $\phi_0 = 1\,V$ has been applied at the bottom wall, creating a potential between electrodes at a distance L. Like the previous test case, no gravitational effects have been considered as the case focuses on the correct implementation of the Maxwell Equations. With this in mind, no initial velocity has been initialized to minimize induced flow effects.
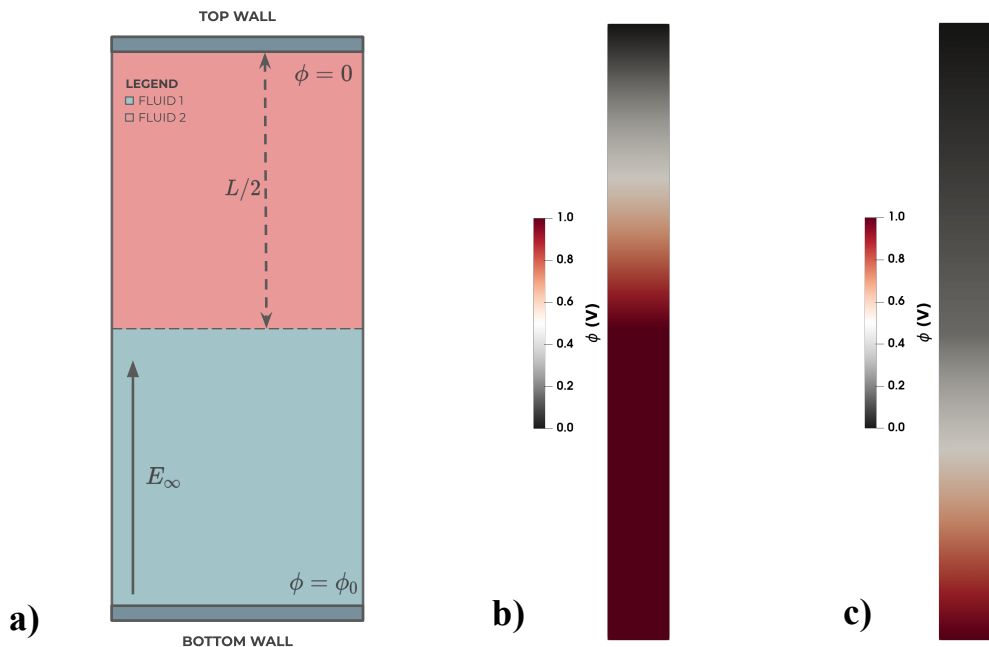
Fig. 15 Planar Layer test case. a) Configuration for Planar Layer validation test. b) Dielectric-conductive case. c) Conductive-conductive case.

According to Roghair et al. and López-Herrera et al., the exact solutions for the two-phase planar

layer cases are given by analytical expressions shown in Table 2 [17,41]. These expressions were obtained

by Taylor in a successful attempt to characterize the stress balance between electric tangential stresses and

hydrodynamic stresses existing only in viscous fluids [35].

Table 2 Analytical Expressions for Planar Layer Test Case

Test Case	Fluid	Potential Distribution, ϕ_D	Electric Field Distribution, E_D
Conductive-Conductive	Fluid 1	$\phi_{D,1} = \dfrac{-2y + R}{1 + R}$	$E_{D,1} = \dfrac{2}{1 + R}$
	Fluid 2	$\phi_{D,2} = \dfrac{R(-2y + 1)}{1 + R}$	$E_{D,2} = \dfrac{2R}{1 + R}$
Dielectric-Dielectric	Fluid 1	$\phi_{D,1} = \dfrac{-2y + Q}{1 + Q}$	$E_{D,1} = \dfrac{2}{1 + Q}$
	Fluid 2	$\phi_{D,2} = \dfrac{Q(1 - 2y)}{1 + Q}$	$E_{D,2} = \dfrac{2Q}{(1 + Q)}$
Conductive-Dielectric	Fluid 1	$\phi_{D,1} = 1$	$E_{D,1} = 0$
	Fluid 2	$\phi_{D,2} = -2y + 1$	$E_{D,2} = 2$

Table 3 Parameters for Planar Layer Test Case

Test Case	Fluid	Conductivity, $\sigma \left(\frac{S}{m}\right)$	Permittivity, $\varepsilon \left(\frac{F}{m}\right)$
Conductive-Conductive	Fluid 1	1	2
	Fluid 2	4	1
Dielectric-Dielectric	Fluid 1	0	1×10^{-12}
	Fluid 2	0	1×10^{-12}
Conductive-Dielectric	Fluid 1	1×10^{-3}	3×10^{-12}
	Fluid 2	0	1×10^{-12}

The results obtained in all 3 cases yield consistent agreement with the analytical solutions, indicating the correct implementation of the electric Poisson equation. Fig. 16 below illustrates these findings in more detail.
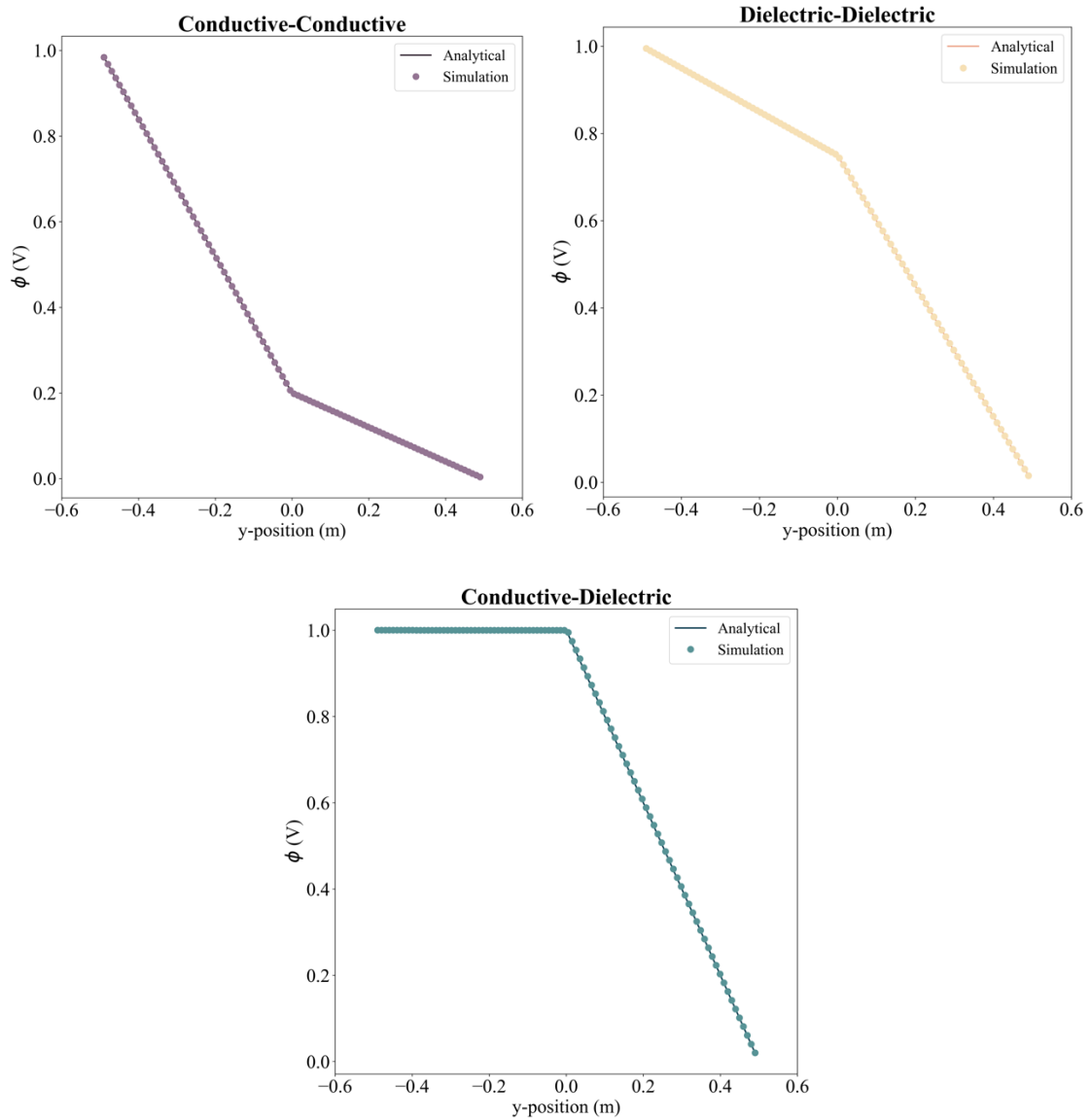
Fig. 16 Analytical comparison of Planar Layer validation test.

V. Results and Discussion

After validating the modifications to the MEPSFoam solver, a discussion of the droplet deformation results is presented in this section. Furthermore, electrospray simulations are introduced to illustrate the reliability and accuracy of the MEPSFoam solver.

A. Droplet Deformation Physics

As an ideal validation test, the physics of droplet deformation under the effects of an electric field have been studied. In 1966, Taylor analyzed this problem and provided an analytical solution for the measurement of the droplet deformation, D_d [35].

$$D_d = \frac{9}{16} \frac{Ca_E}{(2+R)^2} f_d \tag{33}$$

$$f_d = 1 + R^2 - 2Q + \frac{3}{5}(R-Q)\frac{2+3\beta}{1+\beta} \tag{34}$$

The expressions in Eq. 33 and 34 are valid for small deformations only as it was derived by perturbation analysis. In this expression, f_d is known as the discriminating function as it determines the direction of the deformation. When $f_d < 0$, the deformation of the droplet is known to adopt an oblate shape, while a prolate shape occurs when $f_d > 0$. In a prolate shape, the deformation occurs along the same direction as the electric field. Contrastingly, in an oblate deformation, the elongation of the droplet occurs in the direction perpendicular to the external electric field. A point of zero deformation occurs at $f_d = 0$. Please note that this criterion is dependent on the external electric field orientation E_∞.
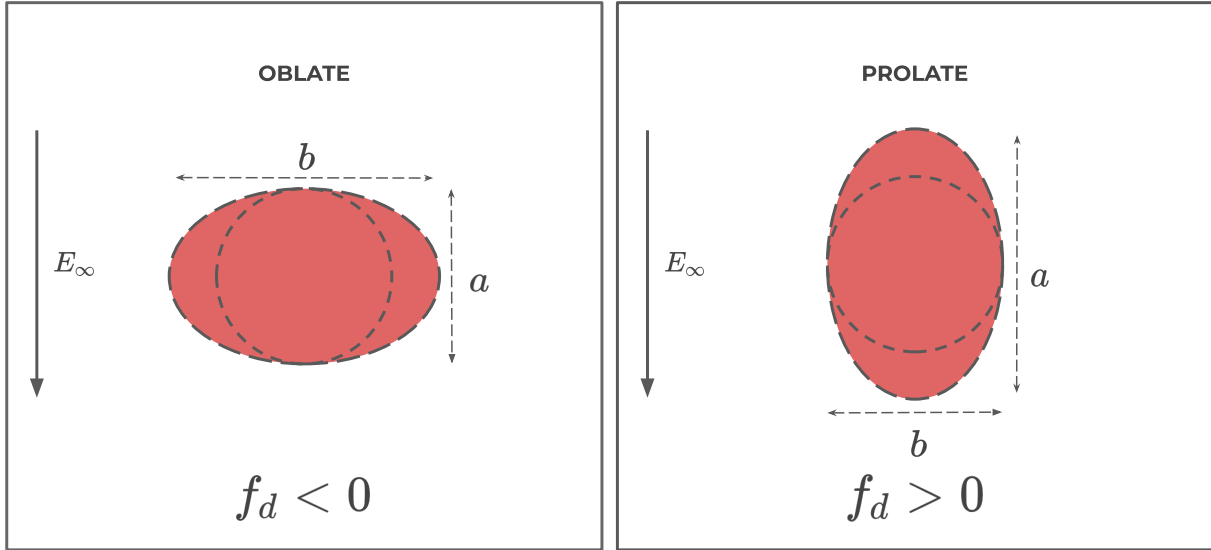
Fig. 17 Droplet deformation as a function of the discriminating function, f_d.

The electric capillary number Ca_E is a good indicator of the relationship between electric forces and surface tension forces. Its definition is given in Eq. 35.

$$Ca_E = \frac{E_\infty^2 \, R_d \, \varepsilon_2}{\gamma} \tag{35}$$

Where R_d is defined as the initial droplet radius, γ is the surface tension coefficient between the two fluids. The external electric field is given by $E_\infty = \frac{\Delta\phi}{L}$. Here, $\Delta\phi$ is the applied electric potential and L is the length between the two electrode plates. The parameters included in Eq. 33 and 34 relate to the properties of both fluids. More precisely, R is equal to the ratio of conductivities between the inner fluid (fluid 1) and the outer fluid (fluid 2). Similarly, the ratios of permittivities and dynamic viscosities are represented by Q and R, respectively. These ratios are defined in Eq. 36 below.

$$R = \frac{\sigma_1}{\sigma_2} \qquad Q = \frac{\varepsilon_1}{\varepsilon_2} \qquad \beta = \frac{\mu_1}{\mu_2} \tag{36}$$

In addition to the evident deformation of the droplet, Taylor discovered a particular fluid behavior inside the droplet. Under the stresses established by the presence of an electric field, a circulatory flow inside the droplet takes place: the existence of four vortices balanced by another four vortices in the outer fluid. exhibits this behavior. As per Taylor's description, sustaining equilibrium necessitates a constant

balance between electric stress and a variable pressure difference on either side of the droplet. This pressure difference is contingent upon fluid motion within and outside the droplet. Additionally, the values of R and Q possess the ability to determine the direction of rotation in the outer vortices. When $R > Q$, the rotation of the top right vortex flows in a clockwise motion, and for $R < Q$, the direction of this same vortex is in the counterclockwise direction.
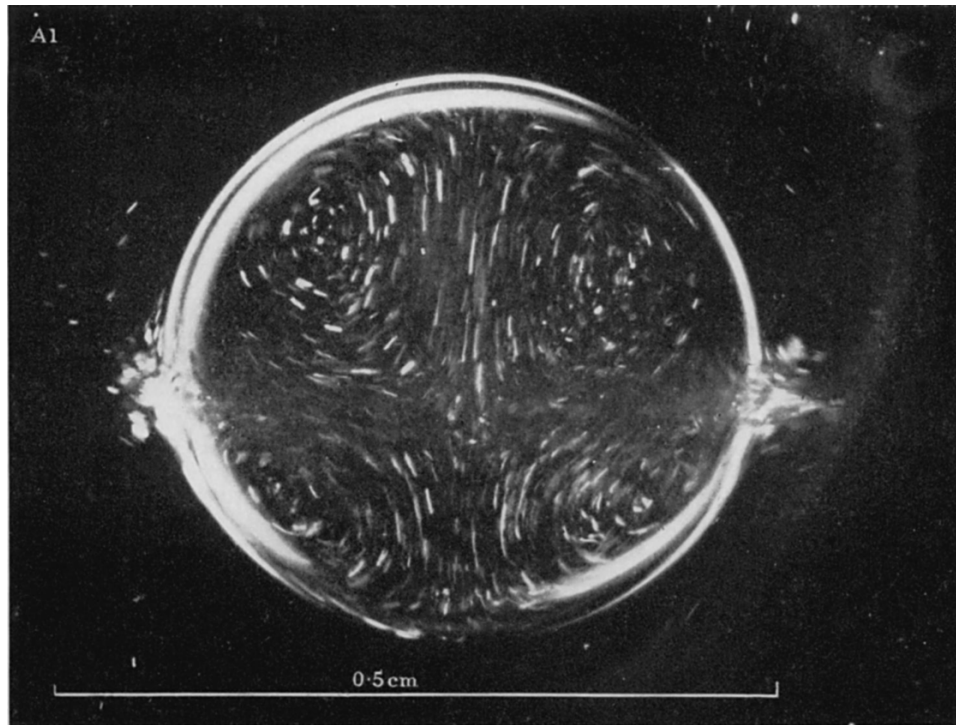
Fig. 18 Circulation inside a silicone oil droplet. Experiment carried out by Taylor [35]. Used with permission of The Royal Society (U.K.) from *Studies in electrohydrodynamics. I. The circulation produced in a drop by an electric field by S.G. Taylor*; permission conveyed through Copyright Clearance Center, Inc.

1. Droplet Deformation Subjected to a Uniform Electric Field

As described in Section III, the deformation of a liquid droplet under the effects of an electric field provides an accurate validation test case to prove the accuracy of the coupling of the electric forces with the existent fluid dynamics involved in the code. In this validation case, a droplet immersed in a background fluid is subjected to an external electric field. A schematic of the case configuration is pictured in Fig. 19. As shown, an electric potential ϕ_0 is applied at the top electrode, forcing the generated electric field to have a downward direction. It is important to note that, in this case, both fluids share the same densities, removing buoyancy effects from the problem. This problem has been widely studied in the literature. Therefore, providing a significant diversity of solutions for comparison [17,40,41,56,57]. Experimentally, this problem was first introduced by Taylor in 1964. For this reason, his work will be of utmost importance to characterize the deformation analysis.
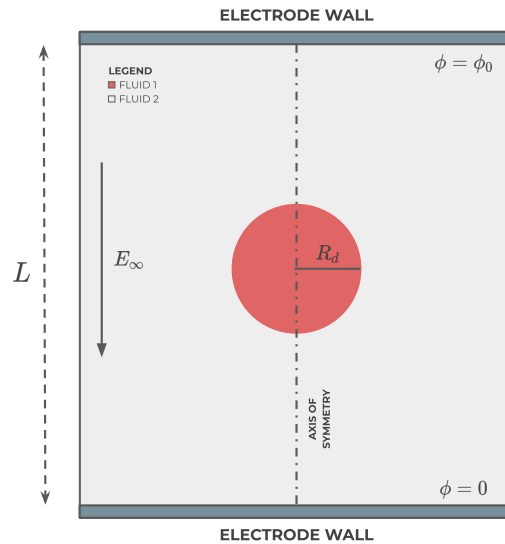
Fig. 19 Axisymmetric setup for droplet deformation case.

For this problem, a two-dimensional axisymmetric configuration with a mesh composed of 25,000 cells has been chosen to simulate the deformation of the droplet. A minimum cell size has been set to 1.953 mm to match the mesh resolution used in Lopez-Herrera's work. This configuration allows us to save computational resources while solving the full tri-dimensional domain when revolved around its axis of symmetry.

36
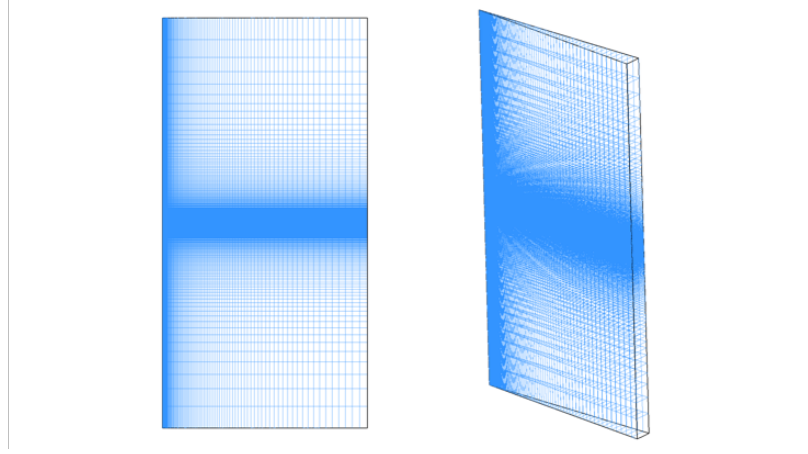
Fig. 20 Front and lateral view of axisymmetric mesh used in droplet deformation case. A grading distribution has been used to focus on maximizing the resolution at the location of the original droplet.

In order to characterize the deformation, an expression defining the aspect ratio of the droplet is used. In Eq. 37, a is defined as the deformation parallel to the external electric field. On the other hand, b is the measurement of the droplet deformation in the direction perpendicular to the electric field. These are shown in more detail in Fig. 17.

$$D_e = \frac{a - b}{a + b} \tag{37}$$

For comparison, the results obtained from the simulation using MEPSFoam have been compared with the analytical solution derived by Taylor (Eq. 33) [35]. This analytical solution was derived by studying the force balance between electrical and capillary stresses. It is important to note that, in order to reach a quantitative agreement with the analytical solution, the domain must comply with the assumption of Stokes flow Taylor suggested in its derivation. In this manner, the domain length for the problem must follow the requirement that $L \gg R_d$ due to confinement effects potentially being significant for the deformation. For this reason, the domain length has been chosen to be $L = 2$.

In his work, Taylor quantified the fluid motion inside and outside the droplets by deriving expressions that explained the velocity components. In the original article, these expressions are given in

spherical polar coordinates. However, the fluid motion expressions are listed below in cartesian coordinates, where the subscripts 1 and 2 refer to the inner fluid and the outer fluid, respectively.

$$u_{1,x} = A\left(\frac{R_d^{-1}}{\sqrt{x^2 + y^2}} - \frac{1}{R_d^3}\sqrt{x^2 + y^2}\right)(2x^2 - y^2) \tag{38}$$

$$u_{1,y} = -Axy\left(\frac{3}{R_d\sqrt{x^2 + y^2}} - \frac{5}{R_d^3\sqrt{x^2 + y^2}}\right) \tag{39}$$

$$u_{2,x} = A\left(\frac{R_d^4}{(x^2 + y^2)^3} - \frac{R_d^2}{(x^2 + y^2)^2}\right)(2x^2 - y^2) \tag{40}$$

$$u_{2,\theta} = 2Axy\left(\frac{R_d^4}{(x^2 + y^2)^3}\right) \tag{41}$$

Where A is described by the same parameters used to derive the droplet diameter solution D_d in Eq. 36.

$$A = -\frac{9}{10}\frac{R_d \varepsilon_2 E_\infty^2}{\mu_2}\frac{R - Q}{(R + 2)^2}(1 + \beta)^{-1} \tag{42}$$

To test the validity of the entire solver, two main parametric studies were considered. First, a study on the effect of the conductivity ratio, R, on the deformation of the droplet. Secondly, a range of different electric capillary numbers were selected to compare with the results from other droplet deformation studies mentioned above. The findings of these two cases are discussed below.

B. Droplet Deformation Discussion: Electric Capillary Number Effects and Conductivity Ratio Parametric Study

Following on the section above, the setup of the problem begins with initializing a circular droplet in the middle of the axisymmetric domain (centered at $L = 2$). The initial droplet radius is set to $R_d = 0.1$. Neumann boundary conditions have been set for the right wall only, while for all other boundaries a combination of Neumann and Dirichlet boundary conditions are used. A voltage is applied to the top

electrode wall, while the bottom electrode wall is set to ground. Similarly, no-slip boundary conditions have been set for these two electrode walls. To comply with the 2D axisymmetric configuration shown in Fig. 19, the left wall (axis of symmetry) has been fixed with a "wedge" boundary condition used for 2D rotationally symmetric cases. In this problem, the right wall is treated as a boundary open to atmospheric conditions. Gravitational effects were purposely neglected in these two cases. Table 4 contains the boundary conditions applied to the computational domain used in this parametric study.

In a similar fashion, the operating parameters utilized for the parametric study of electric capillary numbers, defined as $Ca_E = \frac{E_\infty^2 R_d \varepsilon_2}{\gamma}$, are listed in Table 5. Note that the applied electric potential and capillary number include the ranges that were used for the different cases. The following electric capillary numbers were considered for this study: $Ca_E = 0.001$, 0.004, 0.025, 0.1, 0.225, 0.4, 0.625, 0.9, 1.6, and 2.5. With the exception of the applied electric potential ϕ_0, all other variables were held constant to achieve these values. In order to ensure stability according to the Courant Number, a maximum limit of $Co = 0.5$ was maintained. Given the size of the mesh, a start time step of $\Delta t = 2 \times 10^{-5}$ s was imposed. However, the simulation has been developed to use adaptive time stepping, allowing to remain below the maximum Courant number at all time steps.

Table 4 Boundary Conditions used for Droplet Deformation Case

Boundary	Pressure	Velocity	Electric Potential	Charge Density
Top Electrode	$\nabla p = 0$	$u = (0,0,0)$	$\phi = \phi_0$	$\nabla \rho_E = 0$
Bottom Electrode	$\nabla p = 0$	$u = (0,0,0)$	$\phi = 0\,V$	$\nabla \rho_E = 0$
Right Wall	$p = p_{atm}$	$\nabla u = 0$	$\nabla \phi = 0$	$\nabla \rho_E = 0$
Left Wall (symmetry)	Symmetry (Wedge)	Symmetry (Wedge)	Symmetry (Wedge)	Symmetry (Wedge)

**Table 5 Initial Operating Parameters Matrix for Droplet Deformation – Ca_E Study**

Initial Droplet Radius, R_d	Conductivity Ratio, R	Permittivity Ratio, Q	Viscosity Ratio, β	Applied Electric Potential, ϕ_0	Electric Capillary Number, Ca_E	Surface Tension Coefficient, $\gamma\left(\frac{N}{m}\right)$
0.1	2.5	2	1	0.1-5 V	0.001-2.5	1

For a qualitative analysis at first glance, it is observed that at $Ca_E = 0.625$ (see Fig. 21), the discriminating function f_d is greater than zero, yielding an accurate prolate deformation. The direction of the top right vortex follows the correct direction when $R < Q$.

The results of the parametric study of Ca_E vs Droplet Deformation are shown in Fig. 22. As expected, the deformation of the droplet tends to increase as the electric capillary number is increased. At high capillary numbers, the results start to deviate from the analytical solution. This could potentially be related to the assumption made by Taylor, in which his analytical expression was only valid at small deformations. At $Ca_E > 1$, the deformations begin to be more significant, potentially violating this assumption. For reference, small deformations are defined as deformations below the threshold: $D_e < 0.1$. Moreover, the increase in electric capillary number also indicates an increase in electrostatic stresses in comparison to the surface tension stresses at the interface of the droplet. Thus, suggesting that the deformation will be greater.

Fig. 21 Prolate deformation of droplet at $Ca_E = 0.625$. Left: Streamlines are shown using a Surface Line Integral Convolution (LIC) representation. Right: Iso-contours of charge density around droplet interface.
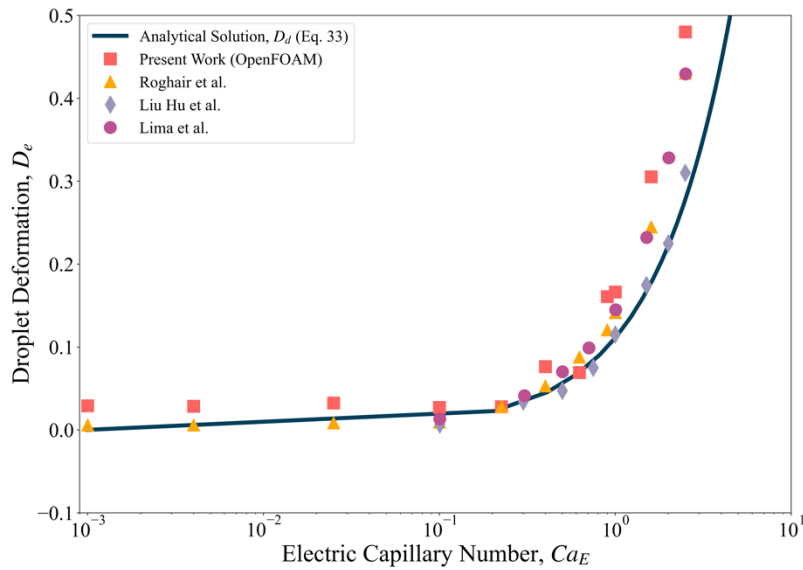
Fig. 22 Droplet deformation for various values of Ca_E. Data from Refs. [41,56,57].

The second parametric study for the droplet deformation problem is the variation of the conductivity ratio, R, at constant operating parameters. Here, the values of $R = 1.81, 2.75, 3.6, 4.2, 5.1,$

6.4, 8.7, and 14.4 were considered. In this case, a constant applied electric potential of $\phi_0 = 2.68\,V$ was used, making the electric capillary number to be $CaE = 0.18$ (see Table 6).

According to theory, the value of $R = 5.1$ indicates no deformation at all, since $f_d = 0$. From the analytical solution, it is expected that the droplet will deform in an oblate shape for values $R < 5.1$, while the deformation will take on a prolate shape for $R > 5.1$. By comparing the results obtained with previous studies of droplet deformation, it is evident that the deformations generated by the MEPSFoam solver follow a comparable trend. However, there is an offset that is apparent at each R value. The exact cause for this effect remains elusive. A probable cause for this discrepancy could be explained by the selection of initial parameters in the configuration of the problem as there is no confirmation that all initial conditions have been exactly replicated from the published work.

Table 6 Initial Operating Parameters Matrix for Droplet Deformation – Conductivity Ratio Parametric Study

Initial Droplet Radius, R_d	Conductivity Ratio, R	Permittivity Ratio, Q	Viscosity Ratio, β	Applied Electric Potential, ϕ_0	Electric Capillary Number, Ca_E	Surface Tension Coefficient, $\gamma \left(\frac{N}{m}\right)$
0.1	1.81-14.4	10	1	2.68 V	0.18	1

At high values of R, deviations from the analytical solution are noticeable. While the small deformation assumption plays a role in explaining this discrepancy, an additional cause could be due to the higher electric stresses experienced by the use of higher conductivity ratios. Thus, increasing the amount of charge accumulation on the droplet interface.
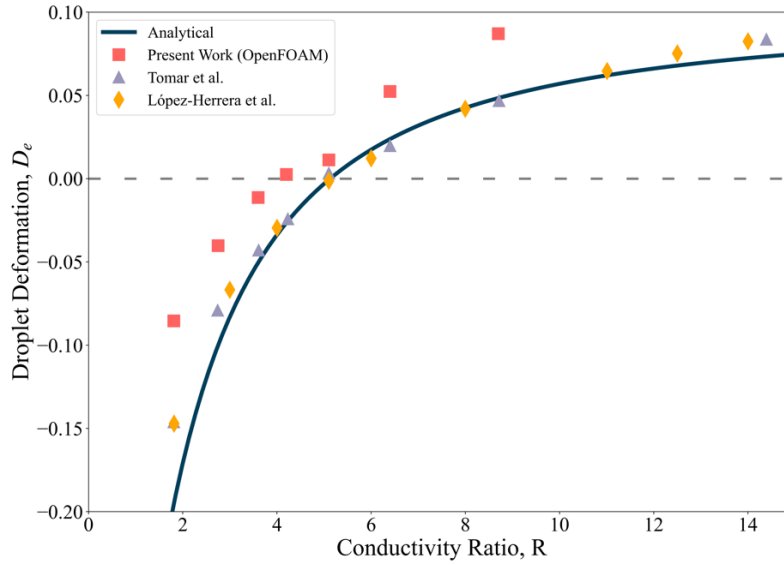
Fig. 23 Droplet deformation for various values of conductivity ratio, *R*. Data from Refs. [17,40].

C. Electrospray Simulations

The ability for the solver to fully capture a steady cone-jet has been comprehensively tested. The aim of this section is to elucidate the behavior of a steady cone-jet as produced by the results of the MEPSFoam solver. To exhibit this behavior, a set of single emitter electrospray simulations using a two-dimensional axisymmetric mesh have been carried out. These simulations aim to reproduce the formation of a Taylor Cone as well as jet breakup as evidenced in experimental trials. A detailed depiction of the electrospray simulation configuration is shown in Fig. 24. Here, numbers next to the components of the electrospray are used to describe the boundaries of the setup. Note that this picture is not to scale, and it is for illustration purposes only.
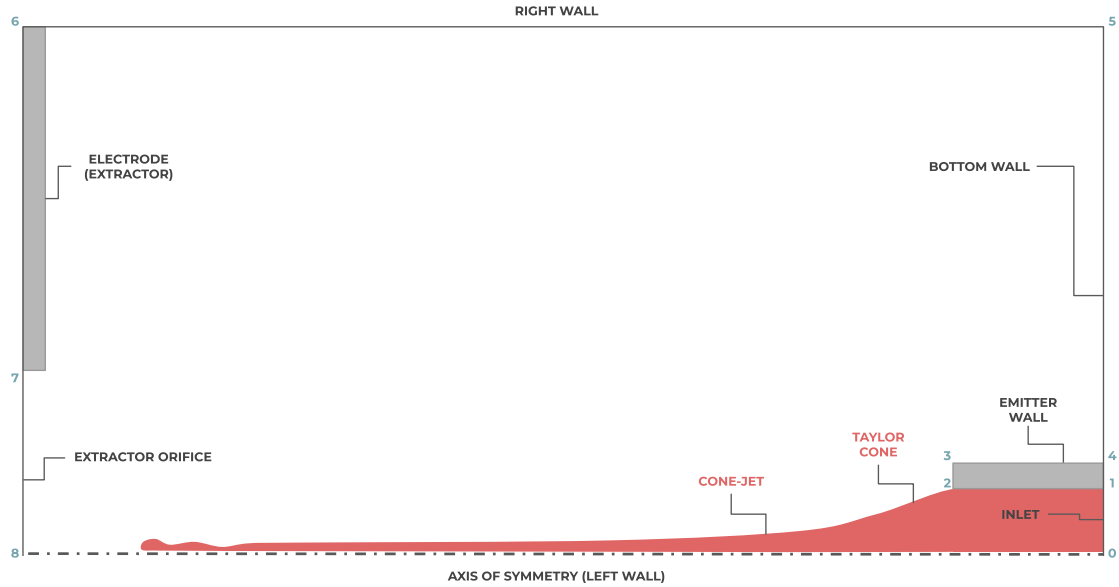
Fig. 24 Electrospray simulation configuration with typical steady cone-jet behavior exhibited in numerical simulations performed by MEPSFoam. Not drawn to scale.

For this problem, a mesh of 364,080 computational cells was selected. Fig. 25 displays the computational mesh selected for all electrospray simulations. This decision was a compromise between run time and performance, as the necessary mesh resolution for measuring the length of a cone-jet proved to be fine in order to avoid substantial numerical diffusion. However, it came at the expense of significantly affecting the amount of time needed to complete a simulation. In this manner, a minimum cell size of 1.27 μm was selected near the emitter exit with mesh grading to decrease the total number of cells in the full computational domain. After noticing pronounced numerical diffusion along the vertical direction, a uniform block of grid cells was extended for 20 mm from the emitter exit. The addition of refined mesh cells at this location included the same minimum cell size as the inlet to ensure sufficient resolution for the measurement of the cone-jet. As shown, a much finer resolution was deliberately specified for the jet region. Due to its conductive properties and its extensive research backing, heptane was selected as the working fluid for all simulations. The properties of heptane were obtained from the work of Tang and Gomez [58]. Although heptane is considered a low electric conductivity liquid, its properties are sufficient to induce a steady cone-jet. For reference, the properties of heptane and the ambient fluid are displayed in Table 7.
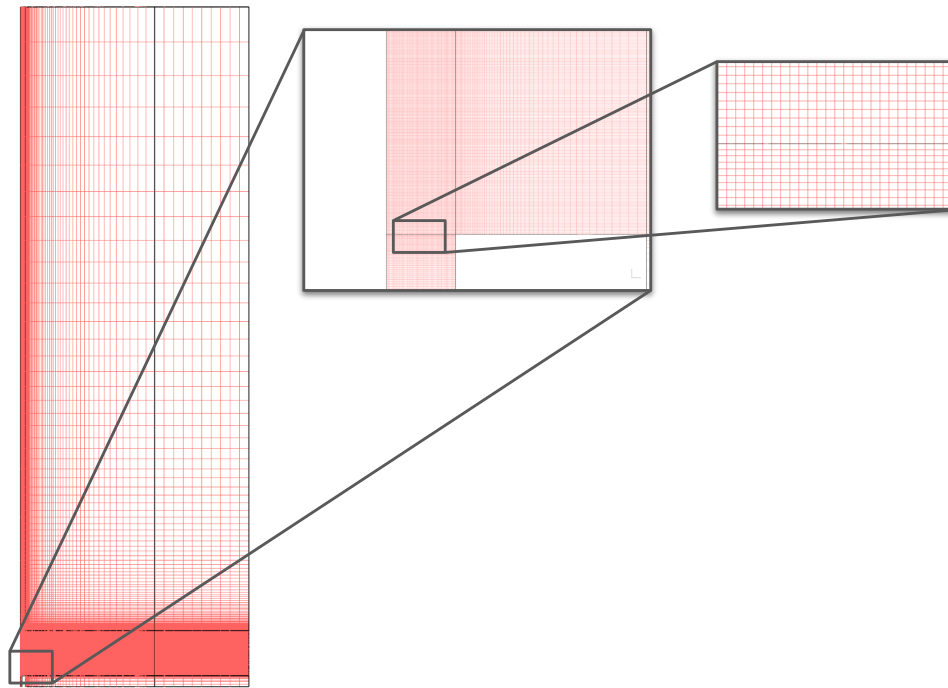
Fig. 25 Computational mesh used for electrospray simulations.

The conditions applied to each boundary are listed in Table 8. Although a velocity has been prescribed at the inlet, in order to speed up the simulations, a separate simulation for the development of the flow has been implemented. This initial run enables the fluid inside the emitter to fully develop and reach the desired U_{max} to match the required flow rate at the exit of the emitter.

Table 7 Fluid Properties used in Electrospray Setup

Fluid	Density, $\rho \left(\frac{kg}{m^3}\right)$	Kinematic Viscosity, $\nu \left(\frac{m^2}{s}\right)$	Conductivity, $\sigma \left(\frac{S}{m}\right)$	Permittivity, $\varepsilon \left(\frac{F}{m}\right)$	Surface Tension Coefficient, $\gamma \left(\frac{N}{m}\right)$
Heptane	684	6.14×10^{-7}	1.4×10^{-6}	1.70886×10^{-11}	0.0186
Air	1.225	1.4939×10^{-5}	1.05×10^{-15}	8.85419×10^{-12}	0.0186

After this simulation has reached convergence, all fields (u, p, α, E) are then mapped onto the full domain, allowing for an optimized run. This is possible due to the use of the mapFields tool in OpenFOAM. All the respective calculations necessary to ensure fully developed flow at the emitter exit were performed separately. An illustration of this method is captured in Fig. 26.

Table 8 Boundary Conditions used for Electrospray Simulations

| Boundary	Section	Distance (mm)	Pressure	Velocity	Electric Potential	Charge Density
Inlet	0-1	0.06	$\nabla p = 0$	$u = \left(0, U_{avg}, 0\right)$	$\nabla \phi = 0$	$\nabla \rho_E = 0$
Emitter	1-4	1	$\nabla p = 0$	$u = (0,0,0)$	$\phi = 0\,V$	$\nabla \rho_E = 0$
Bottom Wall	4-5	20	$p = p_{atm}$	$\nabla u = 0$	$\nabla \phi = 0$	$\nabla \rho_E = 0$
Right Wall	5-6	30.8	$p = p_{atm}$	$\nabla u = 0$	$\nabla \phi = 0$	$\nabla \rho_E = 0$
Top Electrode (Extractor)	6-7	14.39	$\nabla p = 0$	$u = (0,0,0)$	$\phi = \phi_0$	$\nabla \rho_E = 0$
Extractor Orifice	7-8	6	$p = p_{atm}$	$\nabla u = 0$	$\nabla \phi = 0$	$\nabla \rho_E = 0$
Left Wall (symmetry)	8-0	30.8	Symmetry (Wedge)	Symmetry (Wedge)	Symmetry (Wedge)	Symmetry (Wedge)
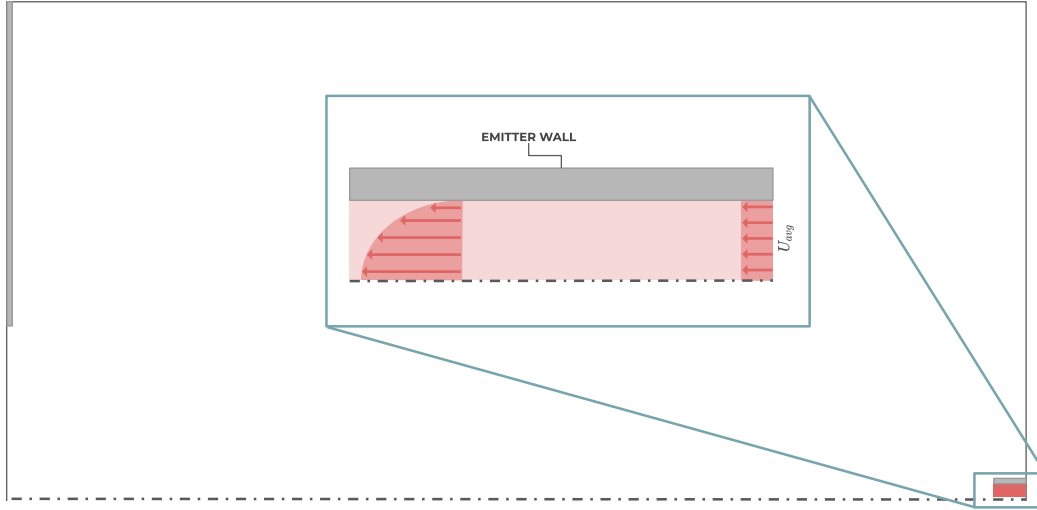
Fig. 26 Illustration of field-mapping of flow development to reach desired flow rate, Q_f. Drawing is not to scale.

1. Role of Liquid Flow Rate in Electrospray Simulation

In this subsection, the role of the liquid flow rate in electrospray dynamics has been investigated. From a qualitative standpoint, for a fixed value of applied voltage, the jet distance will increase as the liquid flow rate increases. Additionally, the cone-jet formation starts at an earlier time step for flows with higher liquid flow rate, compared to those with lower flow rates. The simulations also show the type of circulation that is normally observed in an electrospray in the steady cone-jet mode. A time comparison of the recirculation inside the jet is shown in Fig. 27. In this figure, a potentially erroneous small pressure artifact can be appreciated in the middle of the liquid jet formation. An identifiable factor contributing to this artifact could be mesh grading introduced at the emitter inlet, where mesh resolution is sacrificed to favor computational efficiency. Another possible cause is the introduction of field mapping at $t = 0\ s$ that creates instability in the first few time steps of the simulation. As time advances, this instability is dampened, and a stable cone begins to form. Moreover, this figure illustrates the formation of a convex meniscus at $t = 0.15\ ms$, the usual cone structure that is observed in experimental works of liquid jets subjected to uniform electric fields before ejecting into a jet. At $t = 12\ ms$, the cone has already transitioned to a full cone-jet. Here, the jet undergoes a decrease and increase in jet diameter, wherein the polarization force intensifies

with an increased concentration of the electric field, and surface tension acts to restore equilibrium on the jet.
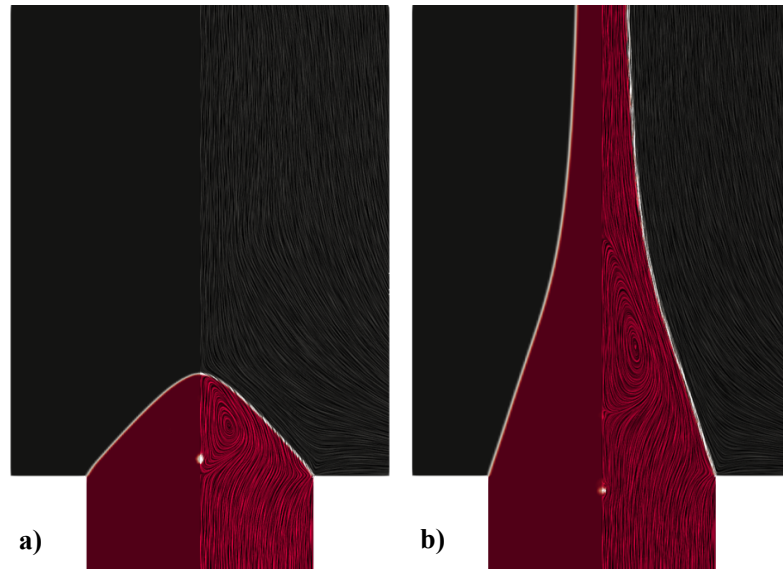
Fig. 27 Recirculation of cone-jet formation at $Q_f = 6.20 \ mL/h$. a) at $t = 0.15 \ ms$
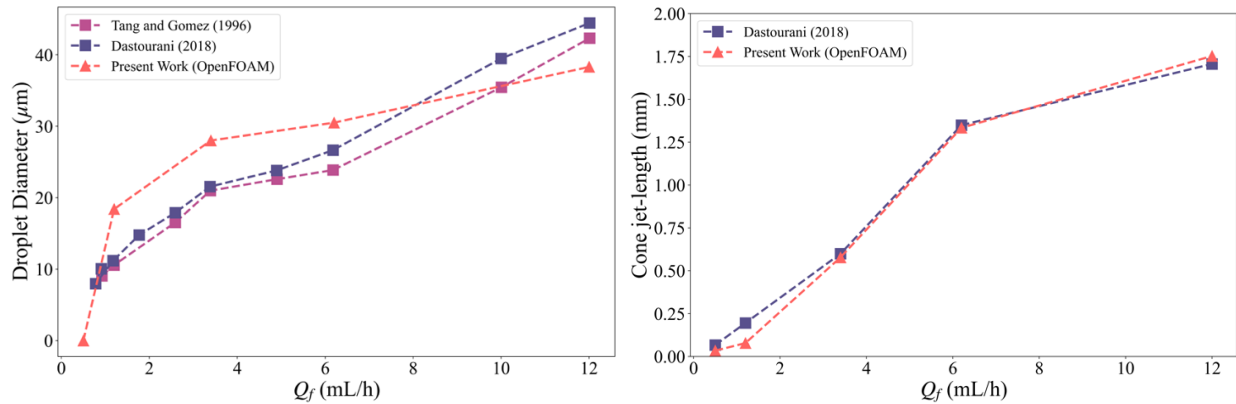
b) at $t = 12 \ ms$.
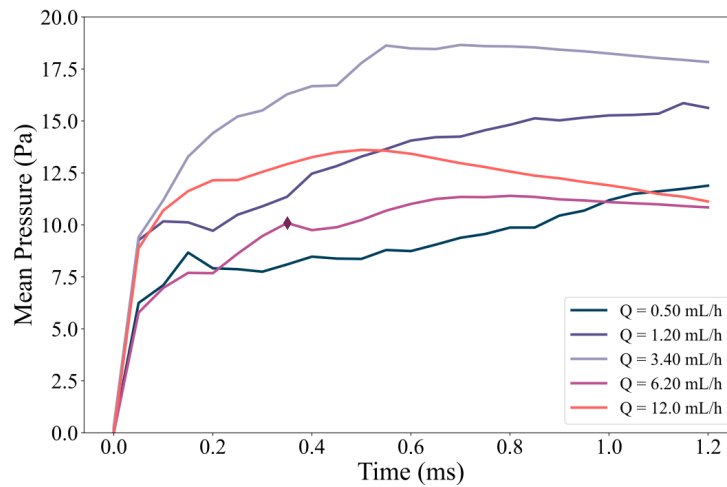
Fig. 28 Mean pressure values for a range of Q_f. Highest local peaks indicate breakup of the jet.

The mean pressure evaluated over the entire computational domain in Fig. 28 demonstrates an interesting trend with regards to the breakup of the jet. A local maximum followed by a local minimum

indicates the time when the jet has broken up into smaller satellite droplets. This behavior is exhibited more prominently in the $Q = 6.20\ mL/h$ curve at the $t = 0.35\ ms$ mark. Furthermore, as evidenced in the plot, larger flow rates such as $Q = 6.20\ mL/h$ and $Q = 12.0\ mL/h$, tend to follow a visibly different trend. This effect can be explained by the mesh resolution at domain areas further from the emitter. At higher flow rates, the cone-jet reaches areas in the computational domain where the mesh resolution is much coarser, yielding significantly higher numerical diffusion that induces erroneous pressure values in the computational cells.

When compared to the experimental data from Tang and Gomez and Dastourani's numerical results, the MEPSFoam produced droplets of higher diameter by a comparable margin [20,58]. The plots in Fig. 29 show that for most flow rates, predicted droplet diameters are larger than those measured experimentally. However, it is evident that the length of the cone-jet as measured from the tip of the emitter agrees reasonably well with the results shared by Dastourani et al. A depiction of the liquid flow rates described in this section are shown in Fig. 30. From the various simulations, it is observed that the breakup caused from jet instabilities occurs at larger distances from the emitter exit as the flow rate is increased.

Fig. 29 Droplet diameter and cone-jet length at $\phi_0 = 4\ kV$, $t = 12\ ms$, and $f = 30$ for various values of Q_f. Data from Refs. [20,58].
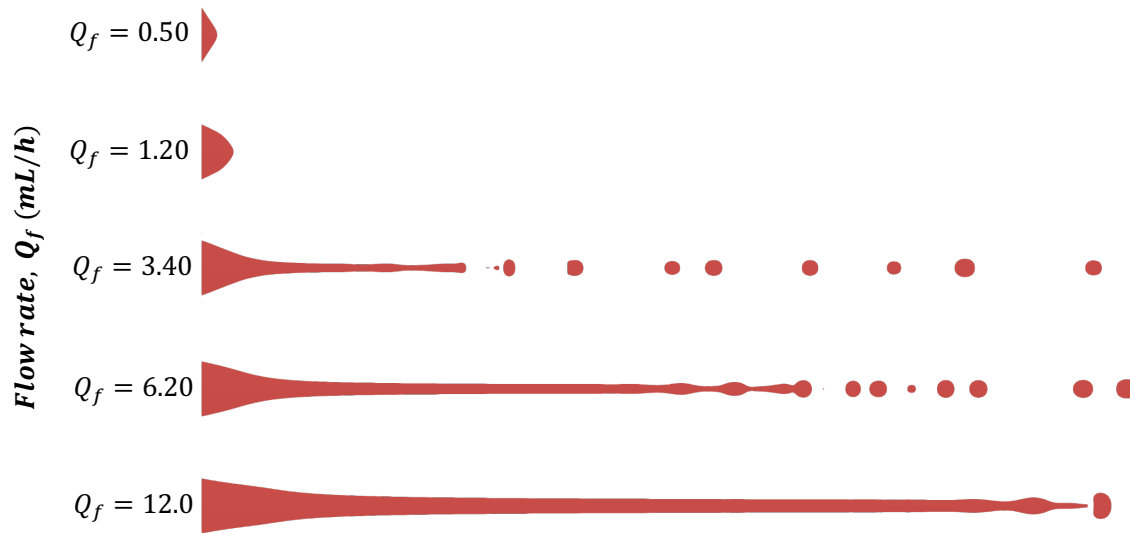
Fig. 30 Cone-jet profiles for various values of Q_f at $t = 12$ s and $f = 1$.

One conjectured explanation for the discrepancies observed in the results could be a product of different measurement techniques. A substantial amount of uncertainty exists in the methods employed by other authors to quantify cone-jet length and droplet diameter. Sufficient clarification on the methodology of these measurements has been consistently left out in the literature and therefore, there is the possibility that the results shown have been measured employing different methods. In this work, measurements have been taken for each single case from the emitter exit to the length in which the jet breaks up into its first droplet.

2. *Role of Applied Electric Potential in Electrospray Simulation*

In addition to studying the effects of liquid flow rate on the formation of cone-jet, an examination of various voltages has been undertaken through parametric analysis. The voltage applied to the system is without a doubt of great importance, as it provides a range of operating limit to produce a steady cone-jet. However, due to the computational limitations of numerical analysis, a study of this kind is better equipped to carry out an analysis of cone-jet development as a function of other parameters such as flow rate, liquid properties, etc. Attempting to find an onset voltage numerically would prove computationally expensive as

a "trial and error" would be required. Although it is theoretically possible, an analysis of this magnitude would require a substantial number of applied voltages to be tested. Analytically, this onset voltage can be estimated using Eq. 1. According to this expression the onset voltage would occur at an applied electric potential of $\phi_0 = 2461.762\ V$.
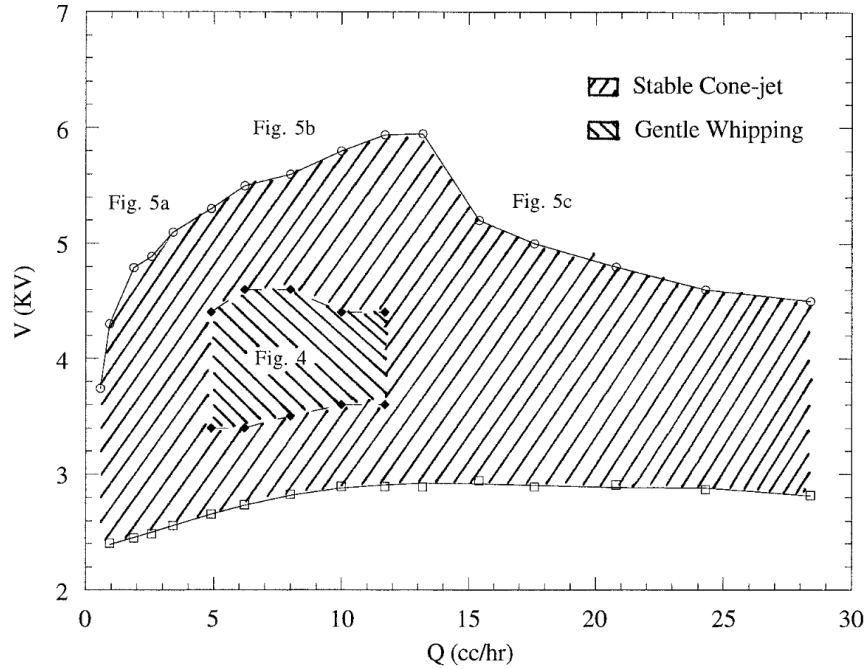
Fig. 31 Steady cone-jet operating regime for Heptane Solution. Courtesy of Tang and Gomez [58].

Given that the stability of an electrospray mode is dependent on the conditions and parameters of a particular fluid, Fig. 31 incorporates the operating regime designed that enables the formation of a stable-cone jet. This illustration delineates the regimes pertinent to the heptane solution utilized in these simulations. Note that the flow rate is given in cubic centimeters per hour, which is equivalent to one milliliter per hour (mL/h).

The figure below (Fig. 32) illustrates a temporal evolution of an electrospray at an applied voltage of 4000 V with a constant flow rate of 3.4 mL/h. A cone formation is evidenced in the beginning of the simulation. As time proceeds, the electric forces in the cone surface overcome the surface tension forces, forcing the cone to eject in a cone-jet shape.
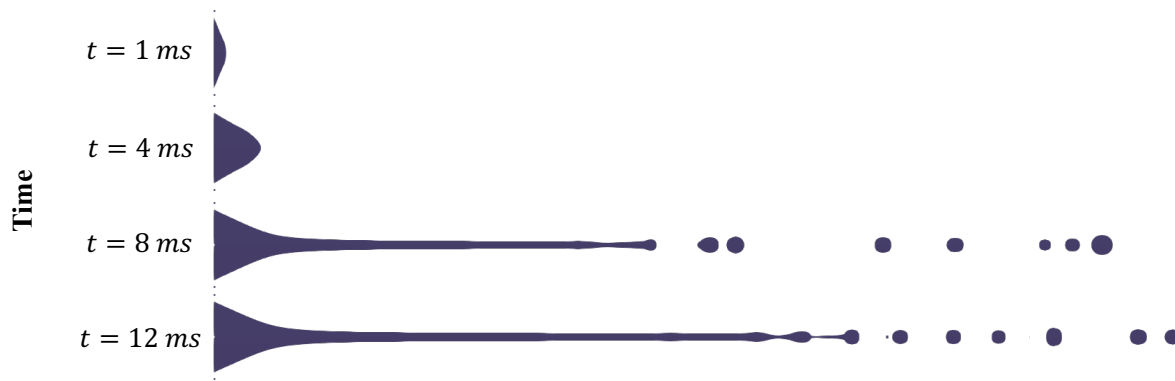
Fig. 32 Transient evolution of electrospray simulations of heptane at $\phi_0 = 4000\ V$, $Q_f = 3.4\ mL/h$.

In Fig. 33, the cone-jet profiles for the different values of applied electric potential are shown. Also, it is observed that the simulations follow the onset voltage calculated at the beginning of this section. As shown, no hydrostatic cone that follows Taylor's theory is formed at $\phi_0 = 2000\ V$ since it is slightly below the onset voltage. At ϕ_0=3000 V, the early onset of a hydrostatic cone can be perceived.

As the electric potential is increased, an earlier formation of the Taylor cone can be observed. At low voltages, the cone begins to form in convex configuration. As the voltage applied to the system is increased, the cone portion of the cone-jet tends to adopt a sharper convex appearance. This is due to the dominance of electric forces over surface tension forces at the interface.

Fig. 33 Cone-jet profiles for various values of ϕ_0 **at** $t = 6\ s$ **and** $f = 1$.
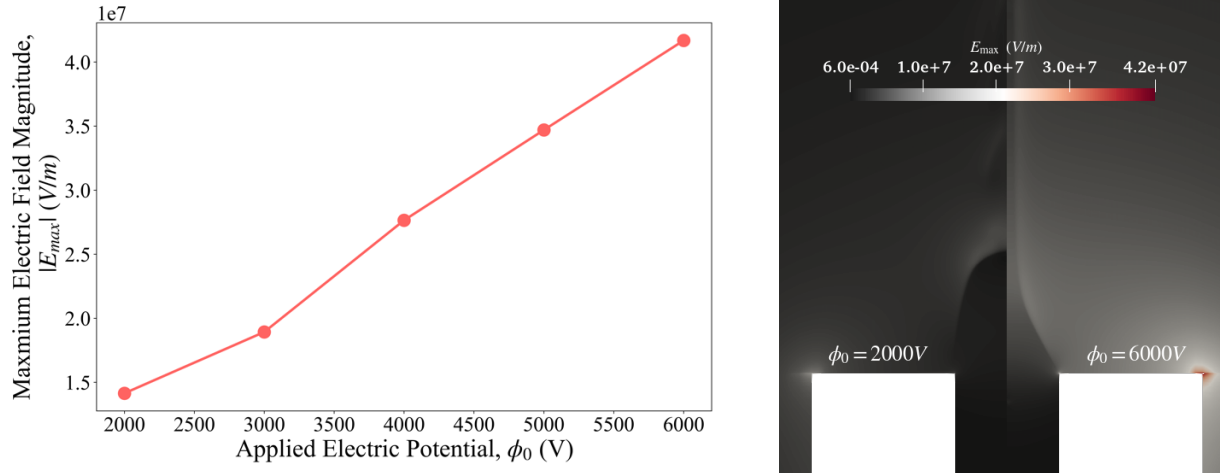
Fig. 34 Maximum electric field magnitude at $Q_f = 3.4\ mL/h$ and $t = 12\ s$ (Left). Comparison of maximum electric field contours for $\phi_0 = 2000\ V$ and $\phi_0 = 6000\ V$ (Right).

A plot of the maximum electric field captured during each simulation is represented in Fig. 34. It is clear that, for the cases evaluated, the maximum electric field follows a linear trend with an increase in applied electric potential, as defined in Eq. 18. As pictured in the image on the right, a significant increase of electric presence is seen near the interface of the cone-jet, therefore validating the voltage effects on the shape of the cone-jet as the applied voltage is varied.

VI. Conclusions and Future Work

This work has focused on the implementation of a numerical solver capable of accurately simulating electrohydrodynamic phenomena. Using the OpenFOAM framework, the existing interFoam solver has been modified to include electrostatic effects in the solution of the Navier-Stokes equations. First, the solution of the Maxwell equations, as implemented in MEPSFoam, was verified by comparing the numerical predictions to analytical solutions in two cases: a planar charge layer and a charge bump decay. To validate the coupling of the electrostatic effects to the Navier-Stokes equations, the simulation results were compared to published measurements of droplet deformation under the effects of a uniform electric field.

The electrospray simulation results confirm that both the liquid flow rate and the applied electric potential affect the shape and onset of the steady cone-jet formation. As the liquid flow rate is increased and the hydrodynamic stresses become more prominent, the cone jet-length increases. Similarly, at higher voltages, the onset of the cone formation appears earlier than at lower voltages.

Significant opportunities lie ahead to advance the research performed in the present work. Firstly, in the context of electric propulsion, a critical area for exploration is the study of multiplexed emitters in both experimental and numerical settings, aiming to further characterize the behavior of neighboring emitters in multiplexed configurations. An analysis of this scale would allow for the quantification of performance of electrospray thrusters in a configuration that is capable of delivering high efficiency propulsion for deep space missions.

Additionally, there is a pressing need to delve into the optimization of the MEPSFoam code. The further analysis of the various numerical schemes applicable could potentially improve the efficiency of the code. This research could benefit from a deeper investigation into more advanced discretization schemes. Some of these advanced schemes include blended divergence schemes, such as LUST (Linear-Upwind Stabilized Transport), and second-order, bounded vector field schemes, such as the SFCD (Self-Filtered

Central Differencing) scheme. This investigation would allow for a detailed comparison of the different numerical schemes and their stability effects on the simulation results. The choice of discretization scheme is known to drastically affect numerical stability and accuracy. Furthermore, attention should be directed towards the inclusion of more sophisticated conductive liquids, potentially leading to the study of high conductivity liquids. Moreover, there is an opportunity to explore the application of many other electrohydrodynamic processes. From printing technologies to medical applications, the robustness of this electrohydrodynamic solver must be explored.

VII. References

[1] Yudistira, H. T., Nguyen, V. D., Dutta, P., and Byun, D., "Flight Behavior of Charged Droplets in Electrohydrodynamic Inkjet Printing," *Applied Physics Letters*, Vol. 96, No. 2, 2010, p. 023503. https://doi.org/10.1063/1.3280077

[2] Fenn, J. B., Mann, M., Meng, C. K., Wong, S. F., and Whitehouse, C. M., "Electrospray Ionization for Mass Spectrometry of Large Biomolecules," *Science*, Vol. 246, No. 4926, 1989, pp. 64–71. https://doi.org/10.1126/science.2675315

[3] Chen, D.-R., and PUI, D. Y. H., "Nanoparticles in Medicine and Environment, Inhalation and Health Effects," 2009, pp. 59–75. https://doi.org/10.1007/978-90-481-2632-3_4

[4] Taylor, G. I., "Disintegration of Water Drops in an Electric Field," *Proceedings of the Royal Society of London. Series A. Mathematical and Physical Sciences*, Vol. 280, No. 1382, 1964, pp. 383–397. https://doi.org/10.1098/rspa.1964.0151

[5] Rayleigh, Lord, "On The Instability of Jets," *Proceedings of the London Mathematical Society*, Vols. s1-10, No. 1, 1878, pp. 4–13. https://doi.org/10.1112/plms/s1-10.1.4

[6] Wright, P. L., and Wirz, R. E., "Multiplexed Electrospray Emission on a Porous Wedge," *Physics of Fluids*, Vol. 33, No. 1, 2021, p. 012003. https://doi.org/10.1063/5.0030031

[7] Jorns, B. A., Gorodetsky, A., Lasky, I., Kimber, A., and Dahl, P., "Uncertainty Quantification of Electrospray Thruster Array Lifetime," *Presented at the 36th International Electric Propulsion Conference*, 2019.

[8] Cisquella-Serra, A., Galobardes-Esteban, M., and Gamero-Castaño, M., "Scalable Microfabrication of Multi-Emitter Arrays in Silicon for a Compact Microfluidic Electrospray Propulsion System," *ACS Applied Materials & Interfaces*, Vol. 14, No. 38, 2022, pp. 43527–43537. https://doi.org/10.1021/acsami.2c12716

[9] Gamero-Castaño, M., and Hruby, V., "Electrospray as a Source of Nanoparticles for Efficient Colloid Thrusters," *Journal of Propulsion and Power*, Vol. 17, No. 5, 2001, pp. 977–987. https://doi.org/10.2514/2.5858

[10] Thuppul, A., Wright, P. L., Collins, A. L., Ziemer, J. K., and Wirz, R. E., "Lifetime Considerations for Electrospray Thrusters," *Aerospace*, Vol. 7, No. 8, 2020, p. 108. https://doi.org/10.3390/aerospace7080108

[11] Jones, J. M., Moeller, T. M., Costa, L., Canfield, B. K., and Terekhov, A., "Numerical Investigation of the Effects of Geometry and Materials on the Onset Voltage of Electrospray Emitters," *Journal of Electrostatics*, Vol. 108, 2020, p. 103487. https://doi.org/10.1016/j.elstat.2020.103487

[12] Juan, L. de, and Mora, J. F. de la, "Charge and Size Distributions of Electrospray Drops," *Journal of Colloid and Interface Science*, Vol. 186, No. 2, 1997, pp. 280–293. https://doi.org/10.1006/jcis.1996.4654

[13] Zeleny, J., "Instability of Electrified Liquid Surfaces," *Physical Review*, Vol. 10, No. 1, 1917, pp. 1–6. https://doi.org/10.1103/physrev.10.1

[14] Morad, M. R., Rajabi, A., Razavi, M., and Sereshkeh, S. R. P., "A Very Stable High Throughput Taylor Cone-Jet in Electrohydrodynamics," *Scientific Reports*, Vol. 6, No. 1, 2016, p. 38509. https://doi.org/10.1038/srep38509

[15] Melcher, J. R., and Taylor, G. I., "Electrohydrodynamics: A Review of the Role of Interfacial Shear Stresses," *Annual Review of Fluid Mechanics*, Vol. 1, No. 1, 1969, pp. 111–146. https://doi.org/10.1146/annurev.fl.01.010169.000551

[16] Lastow, O., and Balachandran, W., "Numerical Simulation of Electrohydrodynamic (EHD) Atomization," *Journal of Electrostatics*, Vol. 64, No. 12, 2006, pp. 850–859. https://doi.org/10.1016/j.elstat.2006.02.006

[17] López-Herrera, J. M., Popinet, S., and Herrada, M. A., "A Charge-Conservative Approach for Simulating Electrohydrodynamic Two-Phase Flows Using Volume-of-Fluid," *Journal of Computational Physics*, Vol. 230, No. 5, 2011, pp. 1939–1955. https://doi.org/10.1016/j.jcp.2010.11.042

[18] Wei, W., Gu, Z., Wang, S., Zhang, Y., Lei, K., and Kase, K., "Numerical Simulation of the Cone–Jet Formation and Current Generation in Electrostatic Spray—Modeling as Regards Space Charged Droplet Effect," *Journal of Micromechanics and Microengineering*, Vol. 23, No. 1, 2013, p. 015004. https://doi.org/10.1088/0960-1317/23/1/015004

[19] Rahmanpour, M., and Ebrahimi, R., "Numerical Simulation of Electrohydrodynamic Spray with Stable Taylor Cone–Jet," *Heat and Mass Transfer*, Vol. 52, No. 8, 2016, pp. 1595–1603. https://doi.org/10.1007/s00231-015-1680-6

[20] Dastourani, H., Jahannama, M. R., and Eslami-Majd, A., "A Physical Insight into Electrospray Process in Cone-Jet Mode: Role of Operating Parameters," *International Journal of Heat and Fluid Flow*, Vol. 70, 2018, pp. 315–335. https://doi.org/10.1016/j.ijheatfluidflow.2018.02.012

[21] Huh, H., and Wirz, R. E., "Simulation of Electrospray Emission Processes for Low to Moderate Conductivity Liquids," *Physics of Fluids*, Vol. 34, No. 11, 2022, p. 112017. https://doi.org/10.1063/5.0120737

[22] Gañán-Calvo, A. M., "Cone-Jet Analytical Extension of Taylor's Electrostatic Solution and the Asymptotic Universal Scaling Laws in Electrospraying," *Physical Review Letters*, Vol. 79, No. 2, 1997, pp. 217–220. https://doi.org/10.1103/physrevlett.79.217

[23] Gamero-Castaño, M., "The Structure of Electrospray Beams in Vacuum," *Journal of Fluid Mechanics*, Vol. 604, 2007, pp. 339–368. https://doi.org/10.1017/s0022112008001316

[24] Eggers, J., and Villermaux, E., "Physics of Liquid Jets," *Reports on Progress in Physics*, Vol. 71, No. 3, 2008, p. 036601. https://doi.org/10.1088/0034-4885/71/3/036601

[25] Pantano, C., Gañán-Calvo, A. M., and Barrero, A., "Zeroth-Order, Electrohydrostatic Solution for Electrospraying in Cone-Jet Mode," *Journal of Aerosol Science*, Vol. 25, No. 6, 1994, pp. 1065–1077. https://doi.org/10.1016/0021-8502(94)90202-x

[26] Mora, J. F. D. L., and Loscertales, I. G., "The Current Emitted by Highly Conducting Taylor Cones," *Journal of Fluid Mechanics*, Vol. 260, 1994, pp. 155–184. https://doi.org/10.1017/s0022112094003472

[27] Gañán-Calvo, A. M., and Montanero, J. M., "Revision of Capillary Cone-Jet Physics: Electrospray and Flow Focusing," *Physical Review E*, Vol. 79, No. 6, 2009, p. 066305. https://doi.org/10.1103/physreve.79.066305

[28] Grace, J. M., and Marijnissen, J. C. M., "A Review of Liquid Atomization by Electrical Means," *Journal of Aerosol Science*, Vol. 25, No. 6, 1994, pp. 1005–1019. https://doi.org/10.1016/0021-8502(94)90198-8

[29] Hirt, C. W., and Nichols, B. D., "Volume of Fluid (VOF) Method for the Dynamics of Free Boundaries," *Journal of Computational Physics*, Vol. 39, No. 1, 1981, pp. 201–225. https://doi.org/10.1016/0021-9991(81)90145-5

[30] Ubbink, O., and Issa, R. I., "A Method for Capturing Sharp Fluid Interfaces on Arbitrary Meshes," *Journal of Computational Physics*, Vol. 153, No. 1, 1999, pp. 26–50. https://doi.org/10.1006/jcph.1999.6276

[31] Hoang, D. A., Steijn, V. van, Portela, L. M., Kreutzer, M. T., and Kleijn, C. R., "Benchmark Numerical Simulations of Segmented Two-Phase Flows in Microchannels Using the Volume of Fluid Method," *Computers & Fluids*, Vol. 86, 2013, pp. 28–36. https://doi.org/10.1016/j.compfluid.2013.06.024

[32] Brackbill, J. U., Kothe, D. B., and Zemach, C., "A Continuum Method for Modeling Surface Tension," *Journal of Computational Physics*, Vol. 100, No. 2, 1992, pp. 335–354. https://doi.org/10.1016/0021-9991(92)90240-y

[33] Saville, D. A., "ELECTROHYDRODYNAMICS:The Taylor-Melcher Leaky Dielectric Model," *Annual Review of Fluid Mechanics*, Vol. 29, No. 1, 1997, pp. 27–64. https://doi.org/10.1146/annurev.fluid.29.1.27

[34] Allan, R. S., and Mason, S. G., "Particle Behaviour in Shear and Electric Fields I. Deformation and Burst of Fluid Drops," *Proceedings of the Royal Society of London. Series A.*

Mathematical and Physical Sciences, Vol. 267, No. 1328, 1962, pp. 45–61.
https://doi.org/10.1098/rspa.1962.0082

[35] Taylor, G. I., "Studies in Electrohydrodynamics. I. The Circulation Produced in a Drop by an Electric Field," *Proceedings of the Royal Society of London. Series A. Mathematical and Physical Sciences*, Vol. 291, No. 1425, 1966, pp. 159–166.
https://doi.org/10.1098/rspa.1966.0086

[36] Mori, Y., and Young, Y.-N., "From Electrodiffusion Theory to the Electrohydrodynamics of Leaky Dielectrics through the Weak Electrolyte Limit," *Journal of Fluid Mechanics*, Vol. 855, 2018, pp. 67–130. https://doi.org/10.1017/jfm.2018.567

[37] Feng, J. Q., and Scott, T. C., "A Computational Analysis of Electrohydrodynamics of a Leaky Dielectric Drop in an Electric Field," *Journal of Fluid Mechanics*, Vol. 311, No. 1, 1996, pp. 289–326. https://doi.org/10.1017/s0022112096002601

[38] Das, D., and Saintillan, D., "Electrohydrodynamics of Viscous Drops in Strong Electric Fields: Numerical Simulations," *Journal of Fluid Mechanics*, Vol. 829, 2017, pp. 127–152.
https://doi.org/10.1017/jfm.2017.560

[39] Feynman, R. P., Leighton, R. B., and Sands, M. L., "The Feynman Lectures on Physics: Mainly Mechanics, Radiation, and Heat," Addison-Wesley, 1964.

[40] Tomar, G., Gerlach, D., Biswas, G., Alleborn, N., Sharma, A., Durst, F., Welch, S. W. J., and Delgado, A., "Two-Phase Electrohydrodynamic Simulations Using a Volume-of-Fluid Approach," *Journal of Computational Physics*, Vol. 227, No. 2, 2007, pp. 1267–1285.
https://doi.org/10.1016/j.jcp.2007.09.003

[41] Roghair, I., Musterd, M., Ende, D. van den, Kleijn, C., Kreutzer, M., and Mugele, F., "A Numerical Technique to Simulate Display Pixels Based on Electrowetting," *Microfluidics and Nanofluidics*, Vol. 19, No. 2, 2015, pp. 465–482. https://doi.org/10.1007/s10404-015-1581-5

[42] Greenshields, C., "OpenFOAM V11 User Guide," The OpenFOAM Foundation, London, UK, 2023.

[43] Greenshields, C., and Weller, H., "Notes on Computational Fluid Dynamics: General Principles," CFD Direct Ltd, Reading, UK, 2022.

[44] Deshpande, S. S., Anumolu, L., and Trujillo, M. F., "Evaluating the Performance of the Two-Phase Flow Solver InterFoam," *Computational Science & Discovery*, Vol. 5, No. 1, 2012, p. 014016. https://doi.org/10.1088/1749-4699/5/1/014016

[45] Holzmann, T., "Mathematics, Numerics, Derivations and OpenFOAM(R)," Leoben, 2016.

[46] Francois, M. M., Cummins, S. J., Dendy, E. D., Kothe, D. B., Sicilian, J. M., and Williams, M. W., "A Balanced-Force Algorithm for Continuous and Sharp Interfacial Surface Tension

Models within a Volume Tracking Framework," *Journal of Computational Physics*, Vol. 213, No. 1, 2006, pp. 141–173. https://doi.org/10.1016/j.jcp.2005.08.004

[47] Roghair, I., Ende, D. van den, and Mugele, F., "An OpenFOAM-Based Electro-Hydrodynamic Model," presented at the 8th International Conference on Multiphase Flow ICMF 2013, Jeju, Korea, May 26 - 31, 2013, 2013.

[48] Greenshields, C., Weller, H., Bainbridge, W., and Kníř, J., "OpenFOAM 8 Released," Jul 22 2020. Retrieved 17 November 2023. https://openfoam.org/release/8/

[49] Nilsson, H., "PhD Course in CFD with OpenSource Software: Programmers Guide," 2008.

[50] Hysing, S., Turek, S., Kuzmin, D., Parolini, N., Burman, E., Ganesan, S., and Tobiska, L., "Quantitative Benchmark Computations of Two-dimensional Bubble Dynamics," *International Journal for Numerical Methods in Fluids*, Vol. 60, No. 11, 2009, pp. 1259–1288. https://doi.org/10.1002/fld.1934

[51] Turek, S., "Efficient Solvers for Incompressible Flow Problems: An Algorithmic and Computational Approach," Springer Berlin, Heidelberg, 2013. https://doi.org/10.1007/978-3-642-58393-3

[52] Turek, S., "On Discrete Projection Methods for the Incompressible Navier-Stokes Equations: An Algorithmical Approach," *Computer Methods in Applied Mechanics and Engineering*, Vol. 143, Nos. 3–4, 1997, pp. 271–288. https://doi.org/10.1016/s0045-7825(96)01155-3

[53] Parolini, N., and Burman, E., "A Finite Element Level Set Method for Viscous Free-Surface Flows," *Applied and Industrial Mathematics in Italy*, 2005, pp. 416–427. https://doi.org/10.1142/9789812701817_0038

[54] John, V., and Matthies, G., "MooNMD – a Program Package Based on Mapped Finite Element Methods," *Computing and Visualization in Science*, Vol. 6, Nos. 2–3, 2004, pp. 163–170. https://doi.org/10.1007/s00791-003-0120-1

[55] Clift, R., Grace, J. R., and Weber, M. E., "Bubbles, Drops, and Particles," 1978.

[56] Hu, L., Fuzhen, C., Ping, W., Fengshan, W., and Hongfu, Q., "Simulating Electrohydrodynamics with Smoothed Particle Hydrodynamics Based on a Charge-Conservative Approach," *Engineering Analysis with Boundary Elements*, Vol. 124, 2021, pp. 41–51. https://doi.org/10.1016/j.enganabound.2020.12.008

[57] Lima, N. C., and d'Ávila, M. A., "Numerical Simulation of Electrohydrodynamic Flows of Newtonian and Viscoelastic Droplets," *Journal of Non-Newtonian Fluid Mechanics*, Vol. 213, 2014, pp. 1–14. https://doi.org/10.1016/j.jnnfm.2014.08.016

[58] Tang, K., and Gomez, A., "Monodisperse Electrosprays of Low Electric Conductivity Liquids in the Cone-Jet Mode," *Journal of Colloid and Interface Science*, Vol. 184, No. 2, 1996, pp. 500–511. https://doi.org/10.1006/jcis.1996.0645